Available online at www.sciencedirect.com
ScienceDirect
ELSEVIER
Icarus 189 (2007) 493–522
ICARUS
www.elsevier.com/locate/icarus

HST observations of azimuthal asymmetry in Saturn's rings

Richard G. French [a,*], Heikki Salo [b], Colleen A. McGhee [a], Luke Dones [c]

[a] *Astronomy Department, Wellesley College, Wellesley, MA 02481, USA*
[b] *Department of Physical Sciences, University of Oulu, PO Box 3000, Finland*
[c] *Southwest Research Institute, Boulder, CO 80302, USA*

Received 7 September 2006; revised 5 February 2007

Abstract

From 378 Hubble Space Telescope WFPC2 images obtained between 1996–2004, we have measured the detailed nature of azimuthal brightness variations in Saturn's rings. The extensive geometric coverage, high spatial resolution ($\sim 300\ \mathrm{km\,px^{-1}}$), and photometric precision of the UBVRI images have enabled us to determine the dependence of the asymmetry amplitude and longitude of minimum brightness on orbital radius, ring elevation, wavelength, solar phase angle, and solar longitude. We explore a suite of dynamical models of self-gravity wakes for two particle size distributions: a single size and a power law distribution spanning a decade in particle radius. From these N-body simulations, we calculate the resultant wake-driven brightness asymmetry for any given illumination and viewing geometry. The models reproduce many of the observed properties of the asymmetry, including the shape and location of the brightness minimum and the trends with ring elevation and solar longitude. They also account for the "tilt effect" in the A and B rings: the change in mean ring brightness with effective ring opening angle, $|B_{\mathrm{eff}}|$. The predicted asymmetry depends sensitively on dynamical ring particle properties such as the coefficient of restitution and internal mass density, and relatively weakly on photometric parameters such as albedo and scattering phase function. The asymmetry is strongest in the A ring, reaching a maximum amplitude $A \sim 25\%$ near $a = 128{,}000$ km. Here, the observations are well-matched by an internal particle density near $450\ \mathrm{kg\,m^{-3}}$ and a narrow particle size distribution. The B ring shows significant asymmetry ($\sim 5\%$) in regions of relatively low optical depth ($\tau \sim 0.7$). In the middle and outer B ring, where $\tau \gg 1$, the asymmetry is much weaker ($\sim 1\%$), and in the C ring, $A < 0.5\%$. The asymmetry diminishes near opposition and at shorter wavelengths, where the albedo of the ring particles is lower and multiple-scattering effects are diminished. The asymmetry amplitude varies strongly with ring elevation angle, reaching a peak near $|B_{\mathrm{eff}}| = 10°$ in the A ring and at $|B_{\mathrm{eff}}| = 15$–$20°$ in the B ring. These trends provide an estimate of the thickness of the self-gravity wakes responsible for the asymmetry. Local radial variations in the amplitude of the asymmetry within both the A and B rings are probably caused by regional differences in the particle size distribution.

Keywords: Planetary rings, Saturn; Radiative transfer

1. Introduction

Saturn's rings exhibit a remarkable photometric property: the brightness of the A ring varies substantially with longitude, with the post-elongation quadrant of each ansa being up to 35% brighter than the pre-elongation quadrant. This prominent large-scale phenomenon is easily detectable even in relatively low resolution images of the rings, and yet it is the consequence of the dynamics of groups of ring particles that are below the resolution even of the stunning close-range Cassini images of the rings taken during Saturn orbital insertion (Porco et al., 2005). The Voyager 1 and 2 encounters provided the first close look at the nature of the asymmetry, such as its amplitude and radial variations throughout the A ring at a variety of viewing geometries (Franklin et al., 1987; Dones et al., 1993), but over a restricted range of wavelength and solar illumination angles. Here, we extend these observational results using a uniform set of Hubble Space Telescope (HST) WFPC2 images taken over the course of a full Saturn season (1996–2004). The

---

[*] Corresponding author.
E-mail address: rfrench@wellesley.edu (R.G. French).

0019-1035/$ – see front matter © 2007 Elsevier Inc. All rights reserved.
doi:10.1016/j.icarus.2007.02.019

broad wavelength coverage (UBVRI), high spatial resolution ($\sim 300\ \mathrm{km\,px^{-1}}$), and excellent photometric accuracy ($\sim 1\%$), combined with dense sampling of the ring brightness surge near opposition, make this a uniquely valuable data set for exploring the detailed character of the azimuthal brightness variations.

We now know that the quadrupole brightness asymmetry is a natural consequence of the competition between the tendency of particles to clump gravitationally and the frustration of this process by tidal shearing interior to the Roche limit. The resulting self-gravity wake structures, analogous to Julian and Toomre (1966) wakes for stellar systems, are tilted in a trailing-arm sense by about 20° relative to circular ring features, and when viewed along their length, the rings appear dimmer because ring particles hide each other and more of the dark sky is visible between particle streams. We have recently carried out photometric modeling of the wakes seen in dynamical simulations, with comparisons to early ground-based and Voyager observations of azimuthal asymmetry (Salo et al., 2004). The success of these models, which reproduced the observed elevation angle dependence of the asymmetry amplitude in ground-based observations, as well as the longitude minima of Voyager observations in both reflected and transmitted light, supports the wake explanation for the asymmetry (Salo and Karjalainen, 1999; Salo et al., 2000; French et al., 2000; Porco et al., 2001). Photometric calculations were based on Monte Carlo modeling of light rays scattered by a system of discrete simulation particles. This technique, as well as its application to azimuthally homogeneous ring models, was described in Salo and Karjalainen (2003). Here, we use the same method for a detailed comparison to the HST data. As in our previous study, we focus primarily on examining the dependence of the expected brightness variations on a suite of dynamical and photometric model values, rather than on trying to obtain exact matches by fine-tuning the parameters of our unavoidably incomplete models.

This paper is organized as follows. In Section 2, we review the key results from previous ground-based and Voyager observations, and then present an overview of the brightness asymmetries detected in the A and B rings from the HST images. Next, in Section 3, we briefly review earlier physical explanations for the brightness asymmetry. We then describe our dynamical models for gravity wakes and our photometric procedures to calculate the resultant wake-driven brightness asymmetry for any given illumination and viewing geometry. In Section 4, we examine the detailed dependence of the asymmetry amplitude and longitude of minimum brightness on elevation angle, solar phase angle, and wavelength. Then, in Section 5, we investigate both observationally and with dynamical models the contrasting nature of the asymmetry throughout the A and B rings, and establish an upper limit on the asymmetry in the more tenuous C ring. Finally, in Section 6, we summarize our key results, compare these to other investigations, and describe directions for future work.

2. Observations of azimuthal asymmetry

2.1. Summary of previous results

Azimuthal brightness variations in Saturn's rings were first noted by Camichel (1958), who found that the A ring leading quadrants (where ring particles have passed elongation) were systematically brighter than the trailing quadrants (where ring particles are approaching elongation). Although the level of variations he found in photographs was large (roughly 10%), this effect had never been reported by visual observers. Camichel's finding was confirmed by Ferrin (1975) and by Reitsema et al. (1976). In particular, the latter study applied a two-dimensional smearing correction to their digitized photographic plates, demonstrating the similarity of the A ring intrinsic brightness variations in the west and east ansae. The smearing model was able to account for the observed variations in the B ring scans, with brightness appearing to increase symmetrically toward the ansae (most likely due to the reduced importance of radial smearing), setting an upper limit of a few percent for any intrinsic B ring azimuthal asymmetry.

In the late 1970s, Lumme and his co-workers carried out detailed studies of the dependence of azimuthal variations on tilt, phase angle, color, and Saturnocentric distance (Lumme and Irvine, 1976, 1979b; Lumme et al., 1977; Thompson et al., 1981; Thompson, 1982). These studies confirmed the nearly perfect $m = 2$ symmetry of the ansae (within 2%) and indicated that the shape and amplitude of A ring variation depends strongly on the ring opening angle, with the mid-A ring amplitude reaching a maximum of ±20% when the ring tilt decreased from 26° to 11.5° (Thompson et al., 1981). For still smaller tilt (6°) the amplitude seemed to decline, but this was somewhat uncertain due to pronounced smearing. There was a suggestion of weaker asymmetry at shorter wavelengths (blue vs red and green), and near opposition at solar phase angle $\alpha < 1°$, compared to $\alpha > 1°$. No asymmetry was detected in the B ring or in the outermost A ring (with 1 and 5% upper limits, respectively). In these observations, the A ring minimum brightness occurred at longitudes of about 20°–25° before elongation, although the scatter in individual scans was large. Large scatter, combined with the small range of phase angles ($\alpha < 6.4°$) accessible in ground-based observations, made it impossible to determine whether the minimum was related predominantly to the observing or illumination direction.

Voyager observations (Franklin et al., 1987; Dones et al., 1993) provided superior radial resolution and a much wider range of observing geometries. A detailed analysis of a sequence of close-range low-phase Voyager images (Dones et al., 1993) showed that the amplitude of variations peaked strongly in the mid-A ring, reaching a full amplitude ($(I_{\max} - I_{\min})/\langle I \rangle$) of about 35% in reflected light at Saturnocentric distance $a =$ 128,000 km (for solar elevation angle $B' \approx 8°$ and viewing elevation angle $B \approx 13°$, with $\alpha = 13°$). In the inner A ring (123,000 km) the amplitude was reduced to about 10%, while near the outer edge (135,000 km) the amplitude was $\sim 15\%$. This radial trend agreed with lower radial resolution scans analyzed in Franklin et al. (1987), obtained from a single image with similar geometry. In the Voyager images, the longitude of minimum brightness of the A ring seemed to be determined primarily by the observer's subring longitude, at least for low phase observations (Dones et al., 1993). At large solar phase angles, the azimuth-dependent indirect illumination due to the planet becomes increasingly important. This makes it very difficult to separate the intrinsic azimuthal reflectivity profile from the ambient scattered Saturnshine, as illustrated by Fig. 4 ($\alpha = 124°$) in Franklin et al. (1987) and Fig. 18 ($\alpha = 147°$) in Dones et al. (1993).

The A ring asymmetry was even stronger in transmitted than in reflected light. For the mid-A ring, Franklin et al. (1987) found the $I_{\max}/I_{\min}$ ratio in unlit-side Voyager images ($B = -29°$, $B' = 8.1°$) to be twice that in reflected light ($B = 11°$, $B' = 7.9°$). At the large phase angle ($\alpha = 94°$) of these transmitted light observations, a significant fraction of the signal was due to Saturn illumination. Franklin et al. (1987) eliminated this component by assuming a Lambert phase function for Saturn itself and using the unlit B ring brightness for normalization. They assumed that no radiation leaked through the B ring, so that its unlit brightness was due solely due to Saturnshine. For transmitted light observations, the location of the minimum was shifted by about 65° relative to low-phase reflected light images. Franklin et al. (1987) anticipated that the longitudes of minima and maxima should reverse between lit and unlit observations, and they attributed the difference between the observed 65° and expected 90° shift to the high phase angle. For the B ring, no detailed asymmetry analysis of the Voyager images has been carried out, primarily because of the presence of prominent spokes at that time. The single low-phase scan for the mid-B ring (109,000 km) presented in Franklin et al. (1987) showed no systematic asymmetry, although the noise level was relatively high (about 5%).

2.2. *Hubble Space Telescope observations*

The high resolution Voyager 1 and 2 images provided measurements of longitudinal brightness variations of the rings over a broad range of solar phase angles, but at only two relatively low solar illumination angles: $B' = 3.9°$ and 8.0° for Voyager 1 and Voyager 2, respectively (Dones et al., 1993). From 1996 to 2004, we carried out an observing campaign with HST's WFPC2, optimized to measure precise brightness and color variations of the rings at high resolution ($\sim$300 $\mathrm{km\,px^{-1}}$) over the course of a Saturn season and to sample the entire range of accessible solar phase angles. We adopted a uniform observing strategy throughout, so as to minimize sources of systematic error when comparing images from different epochs. The observing period covered eight oppositions, enabling us to measure the near-opposition surge at a variety of ring opening angles.

These observations have been used to study Saturn's G ring (Lissauer and French, 2000), satellite astrometry (McGhee et al., 2001; French et al., 2006), the ring opposition effect (Poulet et al., 2002), ring color (Cuzzi et al., 2002), the orbits of Prometheus and Pandora (French et al., 2003), spokes in Saturn's B ring (McGhee et al., 2005), the satellite opposition effect (Verbiscer et al., 2005), Saturn's zonal winds (Sánchez-Lavega et al., 2002, 2003, 2004), and the vertical structure of atmospheric hazes (Pérez-Hoyos et al., 2005). Collectively, these works contain extensive descriptions of the observations that will not be repeated here. For this study, we used 378 UBVRI images of the rings taken with the PC chip of WFPC2. We targeted the east and west ansae separately during a typical "visit"; on average, about seven WFPC2 images were taken of each ansa in the UBVRI filters (F336W, F439W, F555W, F675W, and F814W), as well as in selected other filters.

We took as our starting point the standard pipeline-processed images delivered by the Space Telescope Science Institute. To convert from raw counts (DN) to normalized reflectivity I/F[1], we first scaled each image by a factor involving the product of the solar spectrum, instrumental response, and throughput over the bandwidth of each filter. We took account of the time since the most recent decontamination of the WFPC2 optics for the F255W and F336W images in our data set, and corrected for scattered light from the planetary disk and the rings themselves by deconvolving a model point spread function (PSF) for each image. Additional details are given by Cuzzi et al. (2002). This compensation scheme was very effective in removing spurious azimuthal ring brightness variations caused by scattered light from the rings and planet that was present in the broad, faint wings of the PSF.

From our set of photometrically calibrated images, we next corrected for geometric distortion using the wavelength-dependent Trauger et al. (1995) polynomial mapping to convert between raw pixel coordinates and a standard WFPC2 distortion-corrected global coordinate system. To determine the absolute pointing of each frame, we used the Encke Division as a fiducial reference. We iteratively solved for the location of Saturn's center in global coordinates such that radial ring reflectivity scans over a range of longitudes centered on elongation had their minima at the center radius of the Encke Division ($a = 133{,}584$ km). This process converged quickly, and the center positions were accurate to about 0.1 PC px, or $0''.005$ (French et al., 2006).

To allow for easy comparison of radial and azimuthal scans from different images, we reprojected the ring region of each image onto a rectilinear grid (a, θ) as a function of ring plane radius a and longitude θ, measured in a prograde direction from the subobserver point on the near side of the ring. We preserved the observed flux by rebinning each raw image pixel into 20×20 subpixels and mapping them into bins of radial width $\mathrm{d}a = 100$ km and longitudinal extent $\mathrm{d}\theta = 0.1°$. (At $a = 100{,}000$ km, $a\,\mathrm{d}\theta = 175$ km.) As a final step in the geometric registration process, we folded and subtracted the (a, θ) projection of each image and adjusted the radial scale by a linear function of θ to ensure that circular features throughout the entire ring region were aligned at all longitudes. These small corrections (at the subpixel level in the original image) minimized artifacts in azimuthal ring brightness scans caused by slight N–S errors in the derived coordinates of Saturn's center.

---

[1] The wavelength-dependent ring reflectivity, I/F, is the ratio of the ring surface brightness I to that of a perfect, flat Lambert surface at normal incidence $\pi F(\lambda)/\pi$, where $\pi F(\lambda)$ is the solar flux density at Saturn at wavelength λ.

Table 1
Summary of HST/WFPC2 observations

Prog. ID	Cycle	Date	B	B'	B_{eff}	α (°)	$\Delta\lambda_{\odot}$ (°)	$\Delta\theta_{\mathrm{range}}$ (°)	# UBVRI	
									E	W
6806	6	1996 Sep 30	−4.31	−4.73	−4.51	0.46	0.21	20	5	3
6806	6	1996 Oct 14	−3.82	−4.93	−4.30	1.93	1.59	20	5	3
6806	6	1997 Jan 10	−3.72	−6.25	−4.66	5.67	5.11	20	5	3
7427	7*a*	1997 Sep 22	−10.59	−10.01	−10.29	2.00	−1.92	30	5	5
7427	7*a*	1997 Oct 1	−10.28	−10.15	−10.21	0.98	−0.97	30	6	5
7427	7*a*	1997 Oct 6	−10.12	−10.22	−10.17	0.50	−0.49	30	6	5
7427	7*a*	1997 Oct 10	−9.99	−10.28	−10.13	0.30	−0.06	30	5	5
7427	7*a*	1998 Jan 1	−8.88	−11.47	−10.01	6.02	5.53	30	8	5
7427	7*b*	1998 Jul 28	−16.67	−14.38	−15.44	6.26	−6.03	35	5	5
7427	7*b*	1998 Oct 13	−15.57	−15.42	−15.49	1.20	−1.23	35	5	7
7427	7*b*	1998 Oct 18	−15.43	−15.47	−15.45	0.69	−0.71	35	5	5
7427	7*b*	1998 Oct 24	−15.25	−15.56	−15.40	0.32	−0.01	35	5	6
8398	8	1999 Aug 25	−21.05	−19.36	−20.17	6.11	−6.24	38	9	5
8398	8	1999 Nov 3	−19.98	−20.16	−20.07	0.43	−0.39	38	5	9
8398	8	1999 Nov 7	−19.90	−20.20	−20.05	0.30	0.02	38	9	5
8660	9	2000 Aug 4	−24.19	−22.92	−23.54	6.10	−6.47	39	9	5
8660	9	2000 Nov 20	−23.56	−23.83	−23.69	0.27	0.08	39	7	7
8660	9	2000 Nov 24	−23.50	−23.85	−23.67	0.59	0.56	39	7	7
8660	9	2000 Dec 6	−23.33	−23.96	−23.64	1.99	2.11	39	9	0
8802	10	2001 Sep 8	−26.16	−25.71	−25.93	6.37	−7.04	39	5	9
8802	10	2001 Nov 28	−25.90	−26.07	−25.99	0.62	−0.64	39	7	7
8802	10	2002 Jan 31	−25.76	−26.29	−26.03	5.58	6.20	39	5	9
9341	11	2002 Sep 21	−26.37	−26.73	−26.55	6.38	−7.12	39	6	5
9341	11	2002 Nov 30	−26.47	−26.72	−26.59	2.01	−2.23	39	5	5
9341	11	2002 Dec 9	−26.52	−26.72	−26.62	1.00	−1.10	39	5	5
9341	11	2002 Dec 14	−26.55	−26.71	−26.63	0.40	−0.40	39	5	5
9341	11	2002 Dec 16	−26.56	−26.71	−26.64	0.23	−0.20	39	5	5
9341	11	2002 Dec 17	−26.57	−26.71	−26.64	0.15	−0.01	39	5	5
9809	12	2003 Aug 25	−25.41	−26.17	−25.79	5.05	−5.58	39	5	5
9809	12	2003 Dec 5	−25.11	−25.75	−25.42	3.05	−3.34	39	5	5
9809	12	2003 Dec 31	−25.53	−25.61	−25.57	0.08	−0.03	39	5	5
9809	12	2004 Jan 1	−25.54	−25.61	−25.58	0.10	0.07	39	5	5
9809	12	2004 Jan 5	−25.60	−25.59	−25.60	0.50	0.52	39	5	5
9809	12	2004 Mar 29	−26.25	−25.11	−25.67	6.34	6.88	39	5	5

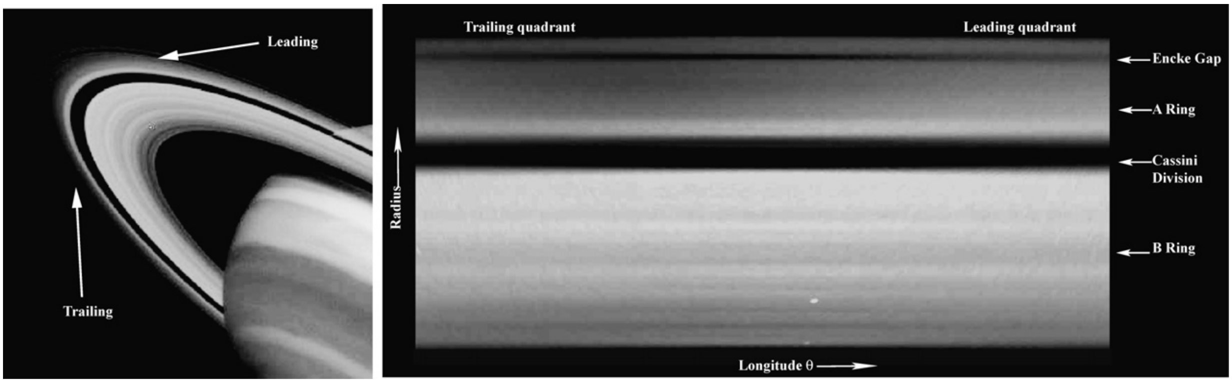

Fig. 1. (Left) The azimuthal asymmetry in the A ring brightness is clearly seen in this contrast-enhanced WFPC2 subframe of the east ansa of Saturn's rings, obtained on 1998 July 28 at a ring opening angle $B = -16.7°$, using the F439W filter. Ring particles revolve clockwise in this image. (Right) The A and B rings are reprojected onto a rectangular coordinate system, with ring longitude θ (spanning ±50° relative to eastern elongation) and ring plane radius r increasing upward. In the A ring, the leading quadrant, where ring particles have recently passed elongation, is markedly brighter than the trailing quadrant, where ring particles are approaching elongation.

Table 1 summarizes the full set of observations used in this paper. For each data set, identified by HST program ID and cycle number, we list the date of each visit, the ring plane opening angle as viewed from the Earth (B) and the sun (B'), the effective ring opening angle B_{eff} (defined below), the solar phase angle α, the difference in (prograde) longitude between the subsolar and subobserver points on Saturn $\Delta\lambda_{\odot}$, the ring longitude relative to elongation $\Delta\theta_{\mathrm{range}}$ (defined below in Eq. (3)), and the number of UBVRI images taken of the east (E) and west (W) ansae during each visit.

Fig. 1 shows a representative subimage of the east ansa of Saturn's rings at moderate ring opening angle ($B = -16.7°$).

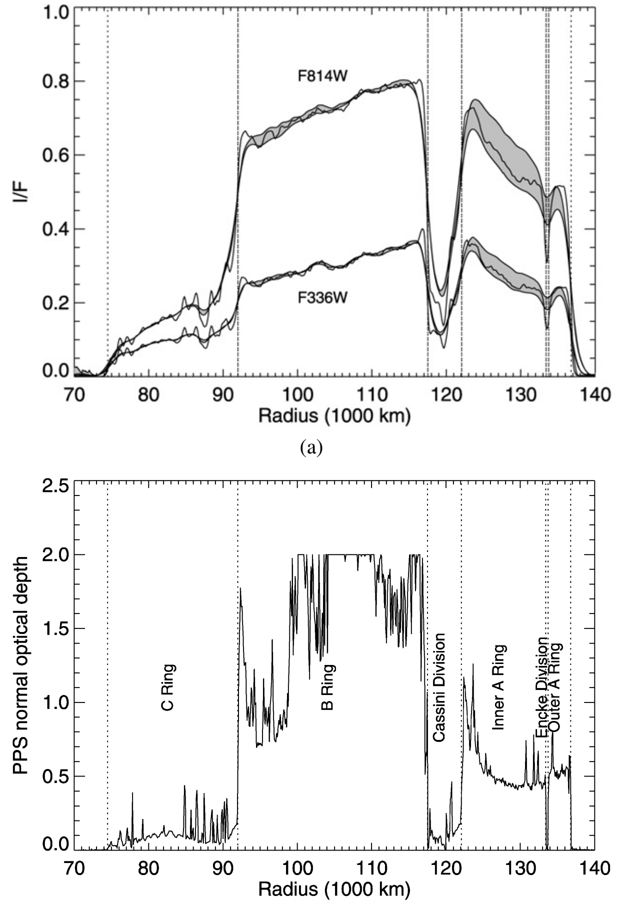

(a)

(b)

Fig. 2. (a) Radial profiles of ring reflectivity I/F at two wavelengths. For each filter, profiles are plotted at ring longitudes of ±20° relative to the ansa and at elongation. The shaded regions identify the brightness contrasts between the leading and trailing profiles. Throughout the A ring, there is a pronounced brightness asymmetry. The effect is much more muted in the B ring, and virtually absent in the C ring. These images were taken on 1997 Oct 10 at a ring opening angle of $B = -10°$. The detailed radial structure of the elongation scan is suppressed by foreshortening in the leading and trailing scans. (b) Radial profile of normal optical depth from the Voyager PPS stellar occultation experiment, shown at 100 km resolution and truncated at $\tau_n = 2.0$. The major ring regions are demarcated by vertical lines. The optical depth in the densest part of the B ring substantially exceeds the values shown here (see Fig. 5 of Colwell et al., 2007), which were limited by the signal-to-noise ratio of the experiment.

Longitudinal brightness variations (marked by the arrows) are prominent in the A ring in the contrast-enhanced image at left and in the reprojected (a, θ) image at right, with the trailing quadrant much dimmer than the leading quadrant. West ansa images show the same behavior, and thus the azimuthal asymmetry is quadrupole. Reprojected images such as that shown in Fig. 1 form the fundamental data set used for our analysis. Fig. 2a shows radial I/F ring reflectivity profiles from two east ansa images taken on 1997 Oct 10 ($B = -10°$) in the F336W and F814W filters, plotted at ring longitudes $+20°$, $-20°$ relative to eastern elongation. The shaded regions bound the brightness differences between the leading (brighter) and trailing (dimmer) profiles. Throughout the A ring, there is a pronounced azimuthal brightness asymmetry; the B ring shows somewhat less, and the C ring almost none at all. The foreshortening of the leading and trailing radial scans suppresses the details of the radial structure of the rings at the relatively low ring opening angle of these images. For comparison, Fig. 2b shows the normal optical depth profile of the rings from the Voyager PPS stellar occultation experiment at 100 km resolution, obtained from the NASA Planetary Data System Rings Node (Showalter et al., 1996).

Henceforth, we will define *geometrically corrected* I/F (see Dones et al., 1993; Cuzzi et al., 2002) as

$$(I/F)_{\mathrm{corr}} = \frac{\mu + \mu'}{2\mu'}(I/F), \tag{1}$$

where $\mu \equiv |\sin B|$ and $\mu' \equiv |\sin B'|$. The effective ring elevation angle, B_{eff}, for observations at slightly different B and B' (note that B and B' must have the same sign), is defined by

$$\mu_{\mathrm{eff}} \equiv \sin B_{\mathrm{eff}} = \frac{2\mu\mu'}{\mu + \mu'}. \tag{2}$$

This correction factor is exact for an optically thick, many-particle thick ring whose reflectivity is due to single scattering, and is quite accurate even when multiple scattering is present (Lumme, 1970; Price, 1973). For large solar phase angle α, there can be significant differences in B and B', and the correction implied by Eq. (1) may amount to as much as 20% for low elevation observations. If uncorrected, this spurious effect of variable observing geometries would overwhelm any true elevation angle dependence of the ring brightness. Such variations in ring brightness with tilt angle are regionally variable, and as will be shown below, also vary with the degree of wake formation. Note that during a single HST observing cycle, B_{eff} is roughly constant, although B and B' may vary. One must also be careful when comparing low α observations at different elevation angles, because strong opposition brightening causes large brightness variations even for small differences in phase angle.

The brightness asymmetry evident in Fig. 1 is present to some degree in every image in our data set. Fig. 3 provides an overview of the observed azimuthal brightness variations from individual images in selected regions of the A and B rings, for a range of ring opening angles. The geometrically corrected I/F at F439W is plotted as a function of ring longitude relative to elongation, averaged over radial ranges as defined in Table 2. To minimize variations in the mean $(I/F)_{\mathrm{corr}}$ due to the opposition surge, images were selected with as close to the same phase angle ($\alpha = 0.3°$) as possible. Thus, most of the variation in the overall ring brightness is due to the ring opening angle (see Cuzzi et al., 2002, for an extensive discussion of this ring tilt effect), rather than a solar phase effect. The scans for $|B_{\mathrm{eff}}| = 4.5°$ were taken shortly after the most recent ring plane crossings in 1995–1996, and at this nearly edge-on geometry the azimuthal scans are resolution limited, particularly in the outer A ring (A135.0) and in narrow B ring features; we include them only for A128.0 and A131.0.[2] With increasing ring open-

---

[2] We adopt a shorthand notation to identify radial regions in the rings, beginning with the ring name and ending with the central radius of the region, in units of 1000 km. See Table 2.

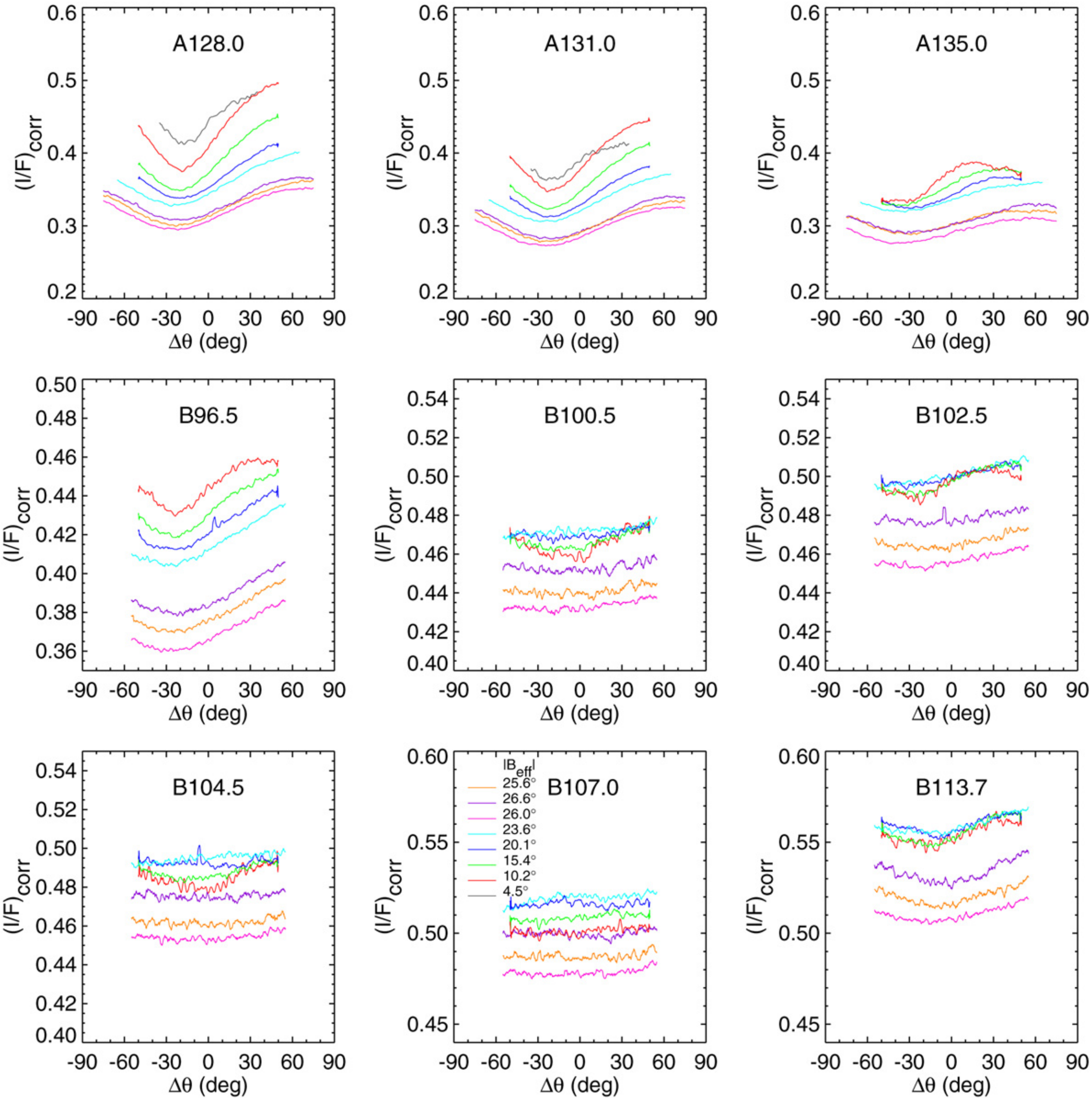

Fig. 3. Azimuthal brightness profiles of selected ring regions. In each panel, the radially averaged longitudinal variation in $(I/F)_{\mathrm{corr}}$ is plotted as a function of longitude relative to elongation, $\Delta\theta$, for a single F439W image at each observed opposition, with solar phase angle $\alpha \sim 0.3°$. The radial extent of each region is given in Table 2. The overall brightness variations for a given region are primarily a tilt effect, as discussed by Cuzzi et al. (2002). The asymmetry is strongest in A128.0 and A131.0, and is clearly detected even for $|B_{\mathrm{eff}}| = 4.5°$, when the rings were nearly edge-on. At this extreme geometry, the radial resolution far from elongation is severely limited and subtle longitudinal brightness variations are at or below the limit of detectability. With increasing ring opening angle, the resolution improves, revealing clearly repeatable variations in the outer A ring (A135.0) and in relatively low optical depth regions of the B ring: B96.5, B102.5, and B113.7. Note the expanded vertical scales for the B ring profiles.

ing angle, the radial resolution far from elongation improves markedly, with reliable repeatable azimuthal variations.

The A ring shows the most dramatic asymmetry, with the brightness minima occurring at ring longitude ~20° before elongation. The brightness then increases gradually with increasing longitude to the end of the reliable region of each azimuthal scan, limited either by resolution (for small $|B_{\mathrm{eff}}|$) or by the disk of the planet itself. Three regions in the A ring were selected for display: A128.0 is centered on a broad region in the middle of the A ring interior to the Encke Division, A131.0 lies just exterior to this region and shows similar strong asymmetry, and A135.0 averages the outer A ring exterior to the Encke Division. Here, the asymmetry is weaker, and for small $|B_{\mathrm{eff}}|$, the strong foreshortening limits the radial resolution away from elongation. The B ring also shows clear evidence of regionally variable azimuthal brightness variations. The asymmetry is strongest near B96.5, more subdued in B102.5 and B113.7, and still weaker or absent in B100.5, B104.5, and B107.5.

These results show that the asymmetry amplitude varies substantially with radius, and to set the stage for comparisons between dynamical models of wakes and the observations, we first present measurements for the A and B rings over the full span of available ring opening angles, B_{eff}. For this purpose, we define the asymmetry amplitude to be

$$A_{\pm\Delta\theta_{\mathrm{range}}} = \frac{I(\Delta\theta_{\mathrm{range}}) - I(-\Delta\theta_{\mathrm{range}})}{I(\Delta\theta_{\mathrm{range}}) + I(-\Delta\theta_{\mathrm{range}})}, \qquad (3)$$

Table 2
Radial ranges in Saturn's rings

Label	Inner radius (km)	Outer radius (km)
C81.5	80,000	83,000
B96.5	95,000	98,000
B100.5	100,000	101,000
B102.5	101,500	103,500
B104.5	104,000	105,000
B107.0	106,500	107,500
B113.7	113,000	114,400
A128.0	127,000	129,000
A131.0	130,000	132,000
A135.0	134,500	135,500

where we introduce the shorthand notation $I \equiv (I/F)_{\text{corr}}$ and $\Delta\theta_{\text{range}}$ is the longitude relative to elongation chosen for each visit to capture the observed asymmetry (see Table 1). In practice, the choice of $\Delta\theta_{\text{range}}$ is restricted to longitudes near the ansa for ring images at low opening angle because the severe foreshortening results in limited radial resolution. This simple definition is useful for an initial exploration of azimuthal brightness variations, and when the asymmetry is weak or absent at some radial locations. Below, we develop alternative definitions that are more suitable when there is a clear quadrupole signature to the asymmetry.

Fig. 4 shows radial profiles of the asymmetry amplitude, $A_{\pm\Delta\theta_{\text{range}}}(r)$, for the A and B rings at eight oppositions, each with a different $|B_{\text{eff}}|$. Each curve represents the average asymmetry for all UBVRI images taken during a given opposition, computed at a radial sampling of 100 km from the reprojected images. The signal-to-noise ratio is markedly improved by averaging over several dozen images, compared to the scans from single images shown in Fig. 3. The Voyager PPS optical depth profile, truncated by noise at $\tau_n = 2.0$, reveals the underlying variations in ring structure. The inner A ring shows strong asymmetry ($A_{\pm\Delta\theta_{\text{range}}} = 0.05$–$0.10$) throughout, reaching a peak near $a = 128{,}000$–$129{,}000$ km. The asymmetry is more difficult to quantify in the resolution-limited narrow A ring exterior to the Encke Division, but even here $A_{\pm\Delta\theta_{\text{range}}} = 0.03$–$0.07$ over the observed range of $|B_{\text{eff}}|$. Individual azimuthal profiles of the B ring (Fig. 3) show regional variations in the strength of the asymmetry. For three zones of moderate optical depth (B96.5, B102.5, and B113.7), there are consistent signatures of enhanced asymmetry at all $|B_{\text{eff}}|$, reaching $A_{\pm\Delta\theta_{\text{range}}} = 0.03$ in the inner B ring and $A_{\pm\Delta\theta_{\text{range}}} = 0.005$–$0.010$ in the two other selected regions. Near the optically thick central region of the B ring (108,000 km), there is a curious (and statistically significant) reversal of the sign of the asymmetry, where the trailing quadrant is brighter than the leading quadrant.

The asymmetry amplitude is strongly dependent on the effective ring opening angle, as illustrated in Fig. 5 for the six shaded regions in Fig. 4. In the A ring, the amplitude peaks at intermediate ring opening angles ($|B_{\text{eff}}| = 10$–$20°$), decreasing sharply for smaller $|B_{\text{eff}}|$ and more gradually for larger values. In the B ring, the variations are more muted, especially where the asymmetry is near the limit of detectability (B113.7), and the peak amplitude is shifted to larger $|B_{\text{eff}}|$ compared to the A ring.

3. Gravity wakes and azimuthal asymmetry

Much of our modeling effort has been devoted to understanding how the observed trends in the photometric behavior of the rings are related to the properties of dynamical wakes and of the ring particles themselves. We begin with a review of previous interpretations of the asymmetry and then describe the connection between gravity wakes and brightness variations of the rings.

3.1. Summary of previous results

The early explanations for the azimuthal brightness asymmetry (e.g., Reitsema et al., 1976) attributed the phenomenon to systematic albedo variations of large synchronously rotating ring particles. Later, it was recognized by Colombo et al. (1976) that the asymmetry could result from small-scale density inhomogeneities in the ring, trailing systematically by about 20°–25° with respect to the local tangential direction. As discussed in Franklin et al. (1987), such trailing inhomogeneities could arise due to dynamical wakes excited around massive particle aggregates (Franklin and Colombo, 1978), or from the superposition of numerous Julian and Toomre (1966) gravity wakes excited by the ring particles themselves (see Franklin et al., 1987; Dones and Porco, 1989). In reality, these concepts represent limiting cases of a continuum of possible configurations, with the same underlying mechanism of kinematic wakes enhanced by the rings' self-gravity. The formation of wakes has been demonstrated in numerous simulation studies, both for dissipative self-gravitating systems leading to continuous regeneration of Julian–Toomre wakes from many moderate-sized particles (Salo, 1992, 1995; Richardson, 1994; Ohtsuki and Emori, 2000; Daisaka and Ida, 1999; see also Toomre and Kalnajs, 1991) and in the case of wakes excited by embedded massive particles (Seiß et al., 2005; see also Karttunen, 1983; Weidenschilling et al., 1984; Franklin et al., 1987). The observed strong asymmetry suggests that the structures responsible for the brightness variations cover a large fraction of the ring area, at least in the mid-A ring, and have a very large intrinsic brightness contrast. This seems to favor the Julian–Toomre type wakes arising among the normal ring particle population over those forced by embedded moonlets, unless the latter are much more abundant than usually assumed. The recent discovery of "propeller" structures in Cassini images (Tiscareno et al., 2006) has placed an upper limit of about one 50–100 m embedded moonlet in the A ring per 1000 km^2. Extrapolating to smaller moonlets with any realistic power law, this implies that there are far too few ring "boulders" to account for the observed asymmetry.

Wakes can produce azimuthal brightness variations because the fractional reflecting surface area is direction-dependent (see Fig. 6 below, and Fig. 1 in Salo et al., 2004). When the wakes

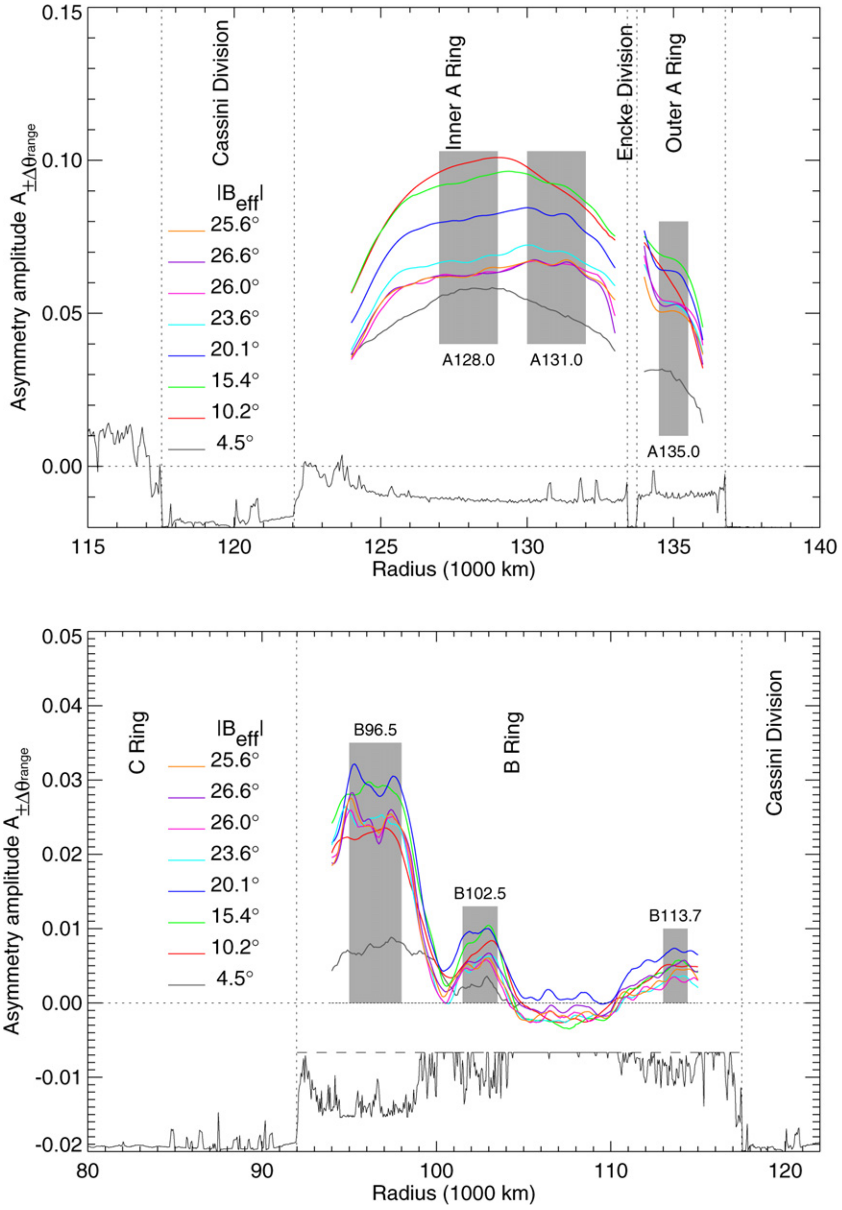

Fig. 4. Radial variation of the amplitude of the azimuthal brightness asymmetry, $A_{\pm\Delta\theta_{\mathrm{range}}}$, in the A ring (upper panel) and the B ring (lower panel), over a range of ring opening angles $|B_{\mathrm{eff}}|$, from UBVRI azimuthal scans of HST images. Results at all solar phase angles during a given Saturn opposition were averaged to obtain the plotted radial variations in asymmetry amplitude. The radial optical depth profile from the Voyager PPS Saturn occultation experiment, truncated by noise at $\tau_n = 2.0$, is shown at the bottom of each panel to reveal underlying ring structure. The vertical shaded bands delimit the radial regions used to compute the variations in asymmetry amplitude with ring opening angle illustrated in Fig. 5. (See Table 1 for the value of $\Delta\theta_{\mathrm{range}}$ used for determining the amplitude for each scan.)

are viewed along their long axes, the rarefied regions between the dense wakes are more visible and the overall brightness is reduced. In the perpendicular viewing direction, the rarefied regions are partially hidden, and thus the rings are brighter. The illumination direction also affects the asymmetry, as does multiple scattering occurring predominantly inside wakes, where the ring particles are most closely packed. Models for the multiple scattering in optically thick ellipsoidal particle "swarms" (Lumme and Irvine, 1979a; Thompson, 1982) could also account for the longitudes of brightness minima and maxima. However, the models in Salo et al. (2004) suggest that the main contribution comes from the singly-scattered component.

3.2. Dynamical models of gravity wakes

In this work, we explore the ability of Julian–Toomre wakes to account for the observed ring brightness asymmetry. Physically, such wakes develop when the rings are on the verge of gravitational instability because of their low velocity dispersion, resulting from the dissipative impacts between particles. Local gravitational collapse is opposed by the particles' random velocity dispersion and by differential rotation, which tends to dissolve any incipient condensations. As long as the velocity dispersion, measured in terms of the dimensionless Toomre parameter (Toomre, 1964),

$$Q = \frac{c_r \kappa}{3.36 G \Sigma} \tag{4}$$

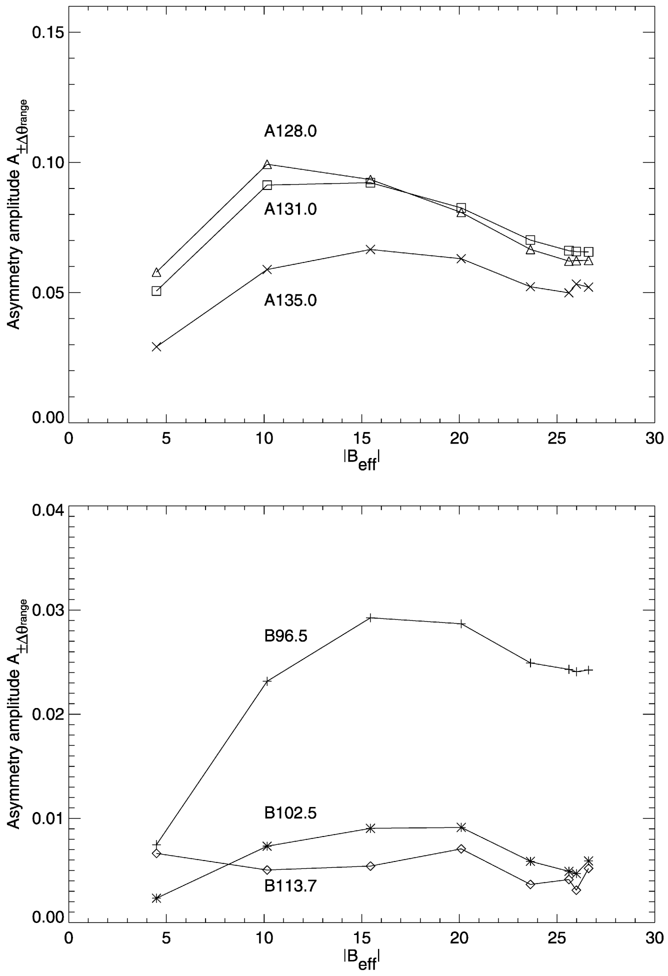

Fig. 5. Variation in the asymmetry amplitude with effective ring opening angle, for selected regions in the A and B rings. In most cases, the asymmetry is strongest at intermediate opening angles $|B_{\rm eff}| \sim 15°$, weakening sharply for $|B_{\rm eff}| < 10°$ and more gradually for $|B_{\rm eff}| > 15°$.

exceeds at least a few times unity, the collective gravitational instability is completely avoided, and the system remains practically uniform. (Here c_r is the radial velocity dispersion, κ is the epicyclic frequency, G is the gravitational constant and Σ the surface density.) This should be the case for low optical depth rings (small Σ), or for rings located near the planet (large κ). However, for larger optical depths or at larger orbital radii, Q could fall below about 2. In this event, the collective gravity and differential rotation produce shearing tilted wake structures, with individual wakes forming and dissolving on a time scale comparable to the orbital period (Salo, 1992; see also Toomre and Kalnajs, 1991). The prominence of these structures stems from the swing amplification process (Goldreich and Lynden-Bell, 1965; Toomre, 1981), which significantly enhances the tiny wakes triggered by each individual particle, leading to significantly stronger structures than would follow from purely kinematic responses. The resulting structures are analogous to the transient wakes produced by orbiting mass enhancements in a stellar disk (Julian and Toomre, 1966; Toomre and Kalnajs, 1991), except that in the rings, dissipative impacts between particles oppose the strong gravitational heating induced by the wakes themselves. This enables a statistical steady-state with velocity dispersion $Q \sim 1$–2, characterized by a continuous regeneration of new transient wakes. Note that the situation $Q < 1$, corresponding to the original Toomre instability criterion against *axisymmetric* collapse, is in practice always avoided.

For Saturn's rings, the approximate condition for the formation of wakes, $Q < 2$, can be written as

$$\tau_{\rm dyn} > \tau_{\rm min} \approx 0.2\left(\frac{a}{10^5\ {\rm km}}\right)^{-3}\left(\frac{\rho}{900\ {\rm kg\,m^{-3}}}\right)^{-1}, \tag{5}$$

or about 0.3–0.1, from the inner C ring to the outer A ring, respectively, for identical particles with the internal density of solid ice [see Salo et al. (2004) for additional details]. Here, $\tau_{\rm dyn}$ is the dynamical, or geometrical, optical depth, defined as the total projected surface area of ring particles per unit area of the rings (Wisdom and Tremaine, 1988; see also Eq. (19), Salo et al., 2004),[3] and $\tau_{\rm min}$ defines a lower limit for the occurrence of wake formation: for $\tau < \tau_{\rm min}$ the surface density of the ring is so small that collective gravity effects are washed out by particle impacts. We emphasize that Eq. (5) is not a strict stability condition, since weak wakes are always present regardless of the value of Q. Nor is there any sudden jump in the wake amplitude at $\tau_{\rm min}$. Rather, Eq. (5) provides an estimate of wake amplitudes large enough to cause noticeable asymmetry. This is a conservative lower limit, since it is based on the assumption of fairly dissipative identical particles that in the absence of self-gravity would concentrate in a very thin ring, just a few particle diameters thick. This is the expected behavior of particles if they follow the Bridges formula (Bridges et al., 1984) for the coefficient of restitution, given by Eq. (8) below. In regions with $\tau_{\rm dyn} > \tau_{\rm min}$, wakes *may* form, depending on the actual particle elasticity, with more elastic impacts implying a dynamically hotter ring and consequently an increased $\tau_{\rm min}$. The formation of wakes is also affected by the particle size distribution, since large particles could provide seeds for strong wakes. This is counteracted, however, by the relatively larger velocity dispersion of small particles, which acts as a stabilizing factor.

The average tilt angle of the transient wakes with respect to the tangential direction is determined by the gradient of the systematic velocity field, corresponding to about 20° for the Keplerian case. This is an effective mean value that takes into account the larger pitch angle of the inner portions of the wakes; the asymptotic pitch angle of the tails of the wakes is ~15°. The typical radial spacing between wakes seen in simulations is close to Toomre's critical wavelength (Toomre, 1964)

$$\lambda_{\rm cr} = 4\pi^2 G\Sigma/\kappa^2, \tag{6}$$

where κ equals the orbital mean motion Ω for the Keplerian case (in Saturn's rings, κ is of order 1% less than Ω due to

---

[3] The dynamical optical depth is constant throughout a given numerical simulation because it is effectively a statement of mass conservation. On the other hand, the photometric optical depth $\tau_{\rm phot}$ (Eq. (20) of Salo et al., 2004) depends on the distribution of ring particles and on the viewing and illumination geometry.

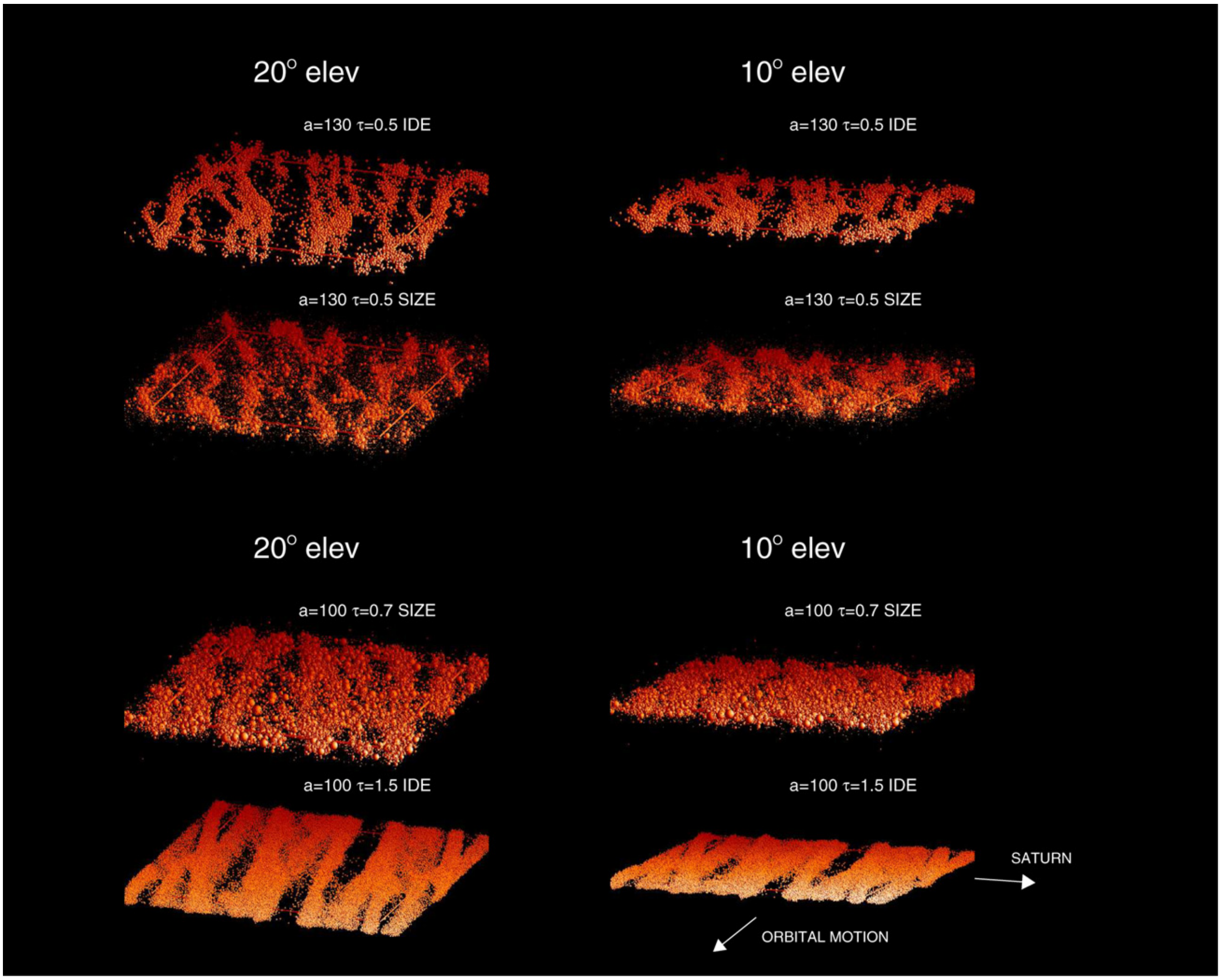

Fig. 6. Examples of dynamical simulations. Upper two rows: the standard identical particle (IDE) and size distribution (SIZE) models representing the A ring ($a = 130{,}000$ km, $\tau_{\rm dyn} = 0.5$). Third and fourth rows: a $\tau_{\rm dyn} = 0.7$ size distribution model for $a = 100{,}000$ km, representing the inner B ring, and a high optical depth ($a = 100{,}000$ km, $\tau_{\rm dyn} = 1.5$) identical particle model representing the dense B ring. Each system is viewed at a ring longitude 250°, from an elevation of 20° (left) and 10° (right), and the size of the calculation region corresponds to $4\lambda_{\rm cr} \times 4\lambda_{\rm cr}$. For the A ring models $\lambda_{\rm cr} = 76$ m, while for the two B ring models $\tau_{\rm dyn} = 0.7$ and 1.5 and $\lambda_{\rm cr} = 48$ and 104 m, respectively. In all cases, the internal density $\rho = 450\ {\rm kg\,m^{-3}}$ and $v_c/v_B = 1$.

Saturn's oblateness). Written for Saturn's rings,

$$\lambda_{\rm cr} = 70\ {\rm m}\left(\frac{a}{10^5\ {\rm km}}\right)^3\left(\frac{\Sigma}{1000\ {\rm kg\,m^{-2}}}\right). \qquad (7)$$

Thus for the A ring with $\Sigma \sim 500\ {\rm kg\,m^{-2}}$ (a typical value based on density wave studies of Rosen et al., 1991), the expected $\lambda_{\rm cr} \sim 50$–100 m.[4]

In the current study, the adopted A ring dynamical simulation parameters are the same as in the identical particle and the size distribution models of Salo et al. (2004): a Saturnocentric distance $a = 130{,}000$ km, internal particle density $\rho = 450\ {\rm kg\,m^{-3}}$, and dynamical optical depth $\tau_{\rm dyn} = 0.5$. The elasticity of particle impacts is described by the normal coefficient of restitution ϵ_n, specifying the ratio of the post- and pre-collisional relative velocity components in the direction joining the particle centers. We adopt the Bridges et al. (1984) velocity-dependent elasticity model,

$$\epsilon_n(v_n) = \min\left[(v_n/v_c)^{-0.234}, 1\right], \qquad (8)$$

where v_n is the normal component of the relative velocity of the impacting bodies and the scale parameter v_c equals $v_B = 0.0077\ {\rm cm\,s^{-1}}$ in Bridges et al.'s measurements. In the identical particle model, the simulations follow $N = 5330$ particles with radii $r = 1.667$ m, while the size distribution model has a power law distribution ${\rm d}N/{\rm d}r \propto r^{-3}$, with $N = 17{,}516$ particles having radii from 0.425 to 4.25 m; both models yield the same $\tau_{\rm dyn} = 0.5$ and surface density $\Sigma = 500\ {\rm kg\,m^{-2}}$. The calculation region covers $4\lambda_{\rm cr} \times 4\lambda_{\rm cr}$, corresponding to $305\ {\rm m} \times 305\ {\rm m}$. For brevity, we will often refer to these as the IDE and SIZE models. Fig. 6 shows representative "snapshots" from both simulations after they have reached a statistical steady state.

In the presence of wakes, the photometric optical depth $\tau_{\rm phot}$ can differ significantly from $\tau_{\rm dyn}$ and be strongly dependent on

---

[4] Lewis and Stewart (2005) have demonstrated that the interplay of satellite forcing and ring self-gravity can lead to larger radial scales, probably accounting for the kilometer-sized wakes seen near the edge of the Encke gap (Porco et al., 2005).

Table 3
Properties of simulated wakes[a]

Model	Region	Simulation	$\tau_{\rm dyn}$		$\tau_{\rm gap}$	H/λ	W/λ	S/λ	$\tan^{-1}(H/S)$	$B_{\rm max}$
I	A128.0	$a = 130{,}000$ km	0.5	IDE	0.10–0.15	1/6	1/4	3/4	13°	11°
II	A135.0	$a = 130{,}000$ km	0.5	SIZE	0.15–0.20	1/4	1/3	2/3	20°	14°
III	B96.5	$a = 100{,}000$ km	0.7	SIZE	0.30–0.40	1/4	1/2	1/2	26°	16°
IV	B113.7	$a = 100{,}000$ km	1.5	IDE	0.10–0.50	1/10	3/4	1/4	22°	12°

[a] H, W, and λ denote the typical vertical thickness, radial width, and radial separation of the wake centers, while $S = \lambda - W$ denotes the width of the gap between the adjacent wakes. The column $\tan^{-1}(H/S)$ gives a rough estimate for the elevation angle at which the interwake gaps become fully visible from all longitudes (with the wake cross-section assumed to be rectangular, as in Colwell et al. (2006, 2007). $B_{\rm max}$ denotes the elevation where the maximum asymmetry amplitude is obtained in the Monte Carlo simulations. In all cases, $v_c/v_B = 1$.

the viewing direction. For the geometry of the Voyager PPS experiment, our IDE and SIZE models predict $\tau_{\rm phot} \approx 0.35$ and 0.4, respectively, in the mid-A ring, slightly below the observed value $\tau_{\rm PPS} \approx 0.45$. Thus, our simulations are in reasonable agreement with a direct Voyager measurement of the photometric optical depth. Furthermore, the trends in $\tau_{\rm phot}$ with ring opening angle and wake longitude from our Monte Carlo models are in qualitative agreement with the Cassini occultation measurements in Colwell et al. (2006).

In addition to the standard A ring IDE and SIZE models, we have explored models with larger $\tau_{\rm dyn}$ and different ϵ_n, for $a = 130{,}000$ km. To investigate the weaker asymmetry observed in the inner B ring, we have also run several simulations for $a = 100{,}000$ km. Finally, we performed a series of simulations with different distances and internal densities, holding other parameters fixed at those of the standard IDE model. For these runs, we used the Bridges et al. (1984) elasticity formula, and scaled the surface density with the optical depth, $\Sigma = 500\frac{\tau_{\rm dyn}}{0.5}\ {\rm kg\,m^{-2}}$. To ensure that the simulations could be reliably compared to each other, a similar $4\lambda_{\rm cr} \times 4\lambda_{\rm cr}$ region was used in all cases, with $\lambda_{\rm cr}$ given by Eq. (7). Snapshots from an $a = 100{,}000$ km SIZE model with $\tau_{\rm dyn} = 0.7$ (to model the inner B ring) and an IDE model with $\tau_{\rm dyn} = 1.5$ (to model the dense middle B ring) are also included in Fig. 6.

The main geometrical characteristics of the models of Fig. 6 are listed in Table 3, including the relative thickness H/λ and width W/λ of typical wakes compared to their radial wavelength $\lambda \sim \lambda_{\rm cr}$, and the optical depth of the interwake gaps, $\tau_{\rm gap}$. We estimated W from visual inspection of several simulation snapshots similar to those in Fig. 6, and determine the gap optical depth from the relative surface area of particles in the low density regions between wakes. We estimated the height H of the wakes from their vertical dispersion $\langle z^2\rangle^{1/2}$, where z is the vertical displacement of a particle from the mid-plane. Table 3 lists the equivalent thickness of a rectangular slab with this dispersion, calculated from $H^2 = 12\langle z^2\rangle$.

Fig. 6 reveals several important characteristics of the dynamical models. For example, the density contrast in the A ring IDE model is much larger than in the corresponding SIZE model, where the small particles partially fill the interwake regions that are much more sparsely populated in the IDE model (see $\tau_{\rm gap}$ in Table 3). Use of more dissipative particles (for example, adopting a constant $\epsilon_n = 0.1$ instead of the Bridges formula) would further increase the wake contrast. Similarly, using a Bridges-type formula with a scale factor $v_c > v_B$ would make the particles more elastic, resulting in reduced wake contrast (see Fig. 11 in Salo, 1995). The snapshots illustrate that the pitch angle is larger for the SIZE model than for the IDE model (~30° instead of ~20°; for a quantitative analysis, see the autocorrelation plots in Salo et al., 2004). The wake contrast is reduced with decreasing Saturnocentric distance, as seen in the two middle rows of Fig. 6, which show the $\tau_{\rm dyn} = 0.5$ and 0.7 SIZE models for the A and B rings. In the B ring model, the wakes are wider relative to their separation than in the A ring (see Table 3). For these relatively low optical depths, the pitch angle of the wakes is similar in the A and B ring models. However, for the B ring model in the bottom row with $\tau_{\rm dyn} = 1.5$, the larger optical depth and the weakened effectiveness of self-gravity because of the stronger tidal field considerably reduce the pitch angle to ~10°. This model also develops axisymmetric overstable oscillations (Schmit and Tscharnuter, 1995). Such behavior occurs in high optical depth simulations (Salo et al., 2001; Schmidt et al., 2001; Schmidt and Salo, 2003), provided that the kinematic viscosity ν increases strongly with optical depth ($\nu \propto {\tau_{\rm dyn}}^{\beta}$, with $\beta \gtrsim 1$).[5] Moderately weak self-gravity, as in the present case, with $\rho = 450\ {\rm kg\,m^{-3}}$ and $a = 100{,}000$ km, promotes this type of viscous behavior, without the wakes being so strong as to suppress the overstable oscillations.

3.3. Photometric modeling

Each dynamical simulation produces a set of particle positions and sizes, enabling us to predict the corresponding ring brightness as a function of viewing geometry. We use the method described in Salo and Karjalainen (2003) and Salo et al. (2004) to perform the photometric calculations, based on following a large number of photons through a ring composed of discrete finite-size particles. The particle field, with periodic planar boundaries, is illuminated by a parallel beam of photons, and the path of each individual photon is followed in detail from one intersection with a particle surface to the next scattering, until the photon escapes the particle field. The new direction after each scattering is obtained via Monte Carlo sampling of the particle phase function. The brightness at a chosen observing direction is obtained by adding together the contributions of all visible individual scatterings. Compared to Monte Carlo estimates based on tabulating the directions of escaped pho-

---

[5] Note that this condition is much more stringent than the $\beta \gtrsim 0$ condition originally proposed by Schmit and Tscharnuter (1995).

tons, this indirect method gives significantly reduced variance. To model the asymmetry, we assume that the particle positions obtained from dynamical wake simulations sample the typical particle distributions at each ring longitude, in a coordinate system aligned with the local radius vector. For a given observing geometry, the brightness is calculated for a range of ring longitudes, each with its own illumination and viewing directions [see Fig. 6 in Salo et al. (2004) for additional details]. To suppress the statistical fluctuations in the dynamical simulations, we average the photometric results for a large number of individual simulation snapshots.

For the particle phase function, we use both the Lambert law

$$P_L(\alpha) = \frac{8}{3\pi}\left[\sin\alpha + (\pi - \alpha)\cos\alpha\right] \tag{9}$$

and a power-law

$$P_{\mathrm{power}}(\alpha) = c_n(\pi - \alpha)^n, \tag{10}$$

where c_n is a normalization constant. For $n = 3.09$, the latter formula gives a good match to the phase function of Callisto and Saturn's inner A ring (Dones et al., 1993), and we will refer to this as the Callisto phase function in the following. In the current study, spherical-particle scattering laws are used both for Lambert and Callisto phase functions, with the photon continuing from the point of scattering. (See Section 3.5 in Salo and Karjalainen (2003) for details of alternative treatments of the particle phase function.) We assume that the Bond albedo $\varpi = 0.5$ when using the Callisto phase function, unless otherwise mentioned. With this value, the modeled ring brightness at low phase angle matches the observations reasonably well. Since the Lambert phase function (with the anisotropy factor $g = -\langle\cos\alpha\rangle = -0.44$) is less backscattering than the Callisto phase function ($g = -0.55$), a larger $\varpi \sim 0.7$ is needed to obtain similar low α brightnesses. As a side effect, the role of multiple scattering is more important in models using the Lambert phase function.

4. Modeling the A ring asymmetry

We begin our development of photometric models of the asymmetry by examining the dependence of the observed amplitude and longitude of minimum brightness on ring elevation, solar phase angle, and wavelength. For these comparisons, we focus our attention on the radial range $a =$ 127,000–129,000 km (A128.0), a relatively smooth A ring region where both Voyager (Dones et al., 1993) and our HST observations (Fig. 4) show the asymmetry to be the strongest. In all cases, we construct models having exactly the same geometry (B, B', α) as the observations in question. We then determine the longitude of minimum brightness and the width of the asymmetry minimum, as described in more detail below.

4.1. *Defining the asymmetry amplitude*

To compare observations and models of the asymmetry, it is useful to have a simple measure of the asymmetry amplitude. This is complicated by limitations in the observations. For example, when computing photometric models for the brightness asymmetry, we have the luxury of predicting the ring brightness at all longitudes, but in the real world, the rings pass in front of and behind Saturn, limiting the observable range of longitudes. Additionally, Saturnshine (reflected sunlight from the planet) illuminates part of the rings, although this effect is negligible at the low phase angles of our data. Finally, at the lowest ring elevations, only the ring region near elongation has sufficient radial resolution for reliable azimuthal scans, further limiting the useful longitude coverage of the observations. This problem is illustrated in Fig. 7, which compares the observed longitude dependence of ring brightness for low and high elevation angles ($B_{\mathrm{eff}} = -4.7°$ and $-25.7°$). To reduce the noise in individual azimuthal scans, such as those shown in Fig. 3, and to provide a more reliable determination of the longitude of minimum brightness, we performed a low-order Fourier fit to the observations over the range of longitudes where the planet does not interfere with the rings and where foreshortening does not seriously limit the radial resolution. The solid lines indicate the Fourier fits to the HST data, and the symbols show the results of a photometric model for the same geometries.

One might define the asymmetry amplitude as

$$A_{\mathrm{asym}} = \frac{I_{\max} - I_{\min}}{I_{\max} + I_{\min}}, \tag{11}$$

where $I_{\min}$ and $I_{\max}$ are the maximum and minimum brightness (cf. Nicholson et al., 2005a), but this otherwise appealing definition is not practical because the longitude near $I_{\max}$ is frequently not observable. Instead, we adopt

$$A_{\Delta\theta} = \frac{I(\theta_{\min} + \Delta\theta) - I(\theta_{\min})}{I(\theta_{\min})} \tag{12}$$

as a measure of amplitude, where $\theta_{\min}$ is the longitude of minimum brightness, and $\Delta\theta$ is chosen such that there is adequate radial resolution in the HST images for a given ring opening angle. We explore the effect of $\Delta\theta$ on the measured asymmetry amplitude by comparing results for $\Delta\theta = 10°, 20°, 30°$, and $40°$, with the corresponding $A_{\Delta\theta}$ denoted by A_{10}, A_{20}, A_{30}, and A_{40}. These amplitudes can be measured reliably for all HST geometries, and this definition enables one to estimate the asymmetry from images that span only a narrow longitude range around the minimum. Note the difference between these amplitudes and the amplitude $A_{\pm\Delta\theta_{\mathrm{range}}}$ used in Figs. 4 and 5, where a different longitude range was used for each elevation.

4.2. *Elevation angle dependence of asymmetry amplitude*

Fig. 8 compares the observed and IDE model amplitudes A_{10}–A_{40} for the mid-A ring (A128.0). The full amplitude $A_{\mathrm{full}} = (I_{\max} - I_{\min})/I_{\min}$ is also shown for $|B_{\mathrm{eff}}| > 15°$, the range of ring tilt for which it can be reliably measured from the images. The shape of the curves depends on the definition of amplitude: A_{10} and A_{20} decrease monotonically with $|B_{\mathrm{eff}}|$, while A_{30} and A_{40} peak near $|B_{\mathrm{eff}}| \sim 10°$. These differences arise from the widening of the asymmetry minimum with increasing elevation. The photometric models match the

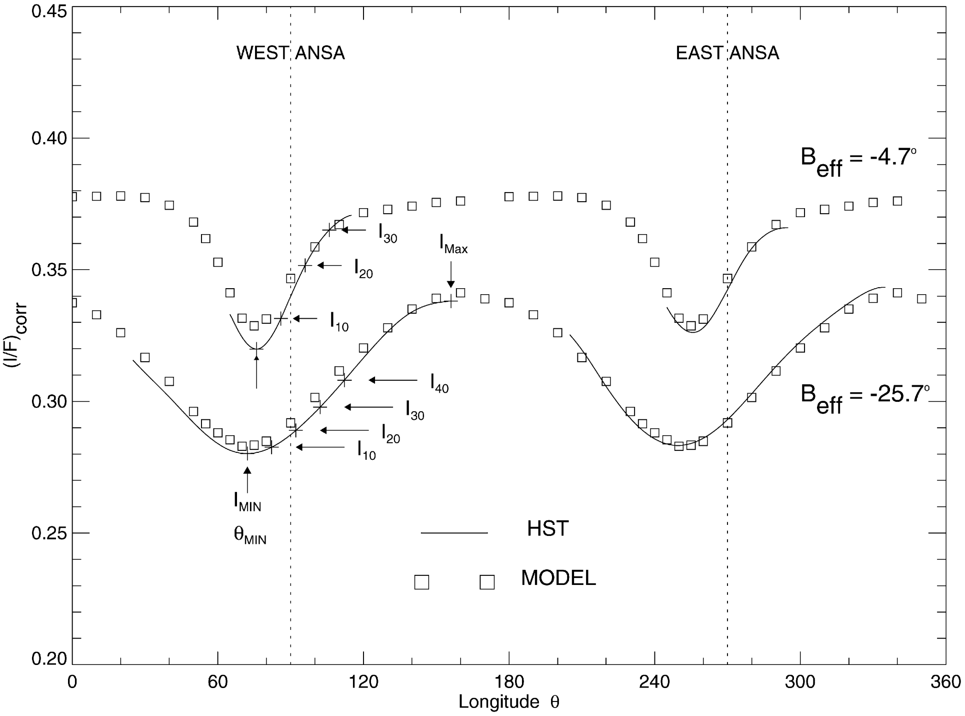

Fig. 7. Illustration of the difference in the longitude ranges observable in Earth-based images at low and high elevation angles. Solid lines show Fourier fits to azimuthal scans from F555W filter images for both east and west ansae, while symbols indicate photometric models for the same geometry ($a = 130{,}000$ km, $\tau_{dyn} = 0.5$, identical particle model, elasticity scale parameter $v_c/v_B = 2$; Callisto phase function with $\varpi = 0.54$ for $B_{eff} = -25.7°$ and $\varpi = 0.46$ for $B_{eff} = -4.5°$). Arrows indicate quantities used in comparisons: the minimum and maximum intensities I_{min} and I_{max}, the longitude of minimum θ_{min}, and the intensities at longitudes 10°, 20°, 30°, and 40° after the minimum. The useful longitude range for the low-elevation scan extends only to about 35° past the minimum brightness, and does not include the longitude at which the model profile reaches a maximum. The scan at larger elevation extends to nearly 80° past the minimum, but even in this case barely reaches the longitude of maximum brightness predicted by the model.

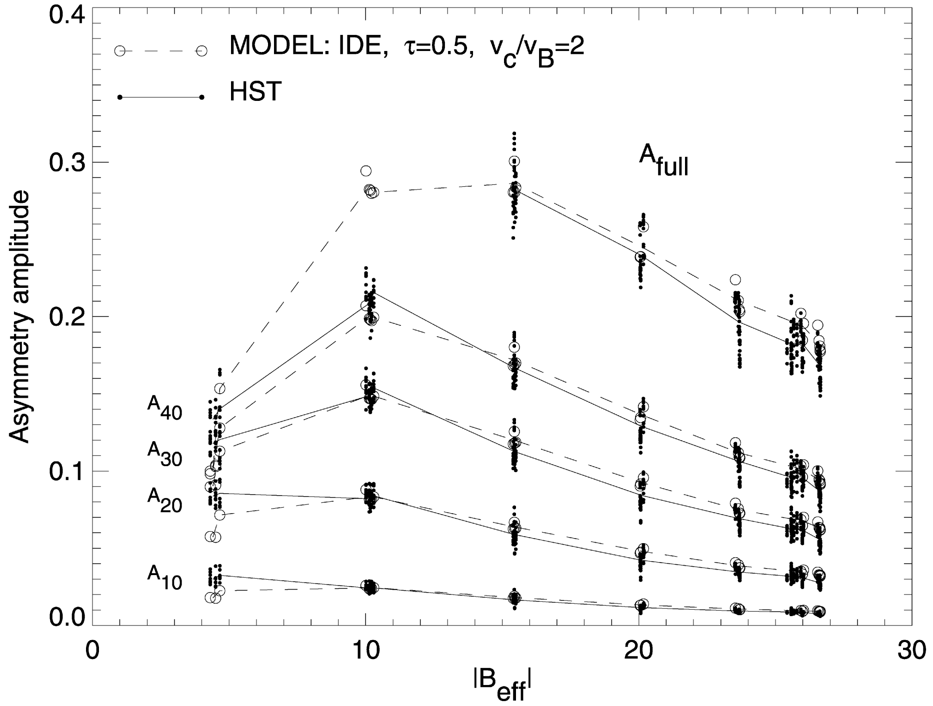

Fig. 8. Comparison of observed and IDE model asymmetry amplitudes for the mid-A ring. Filled symbols show the measured amplitudes for the region A128.0 ($a = 127{,}000$–$129{,}000$ km), using observations at all wavelengths and phase angles. The solid lines connect the mean values of the observations, grouped by ring opening angle. Open symbols (individual models) and dashed lines (similarly grouped according to $|B_{eff}|$) correspond to photometric models constructed for the same geometry. Here, we have used the standard IDE dynamical model, with elasticity parameter $v_c/v_B = 2$, and a Callisto phase function with albedo $\varpi = 0.5$.

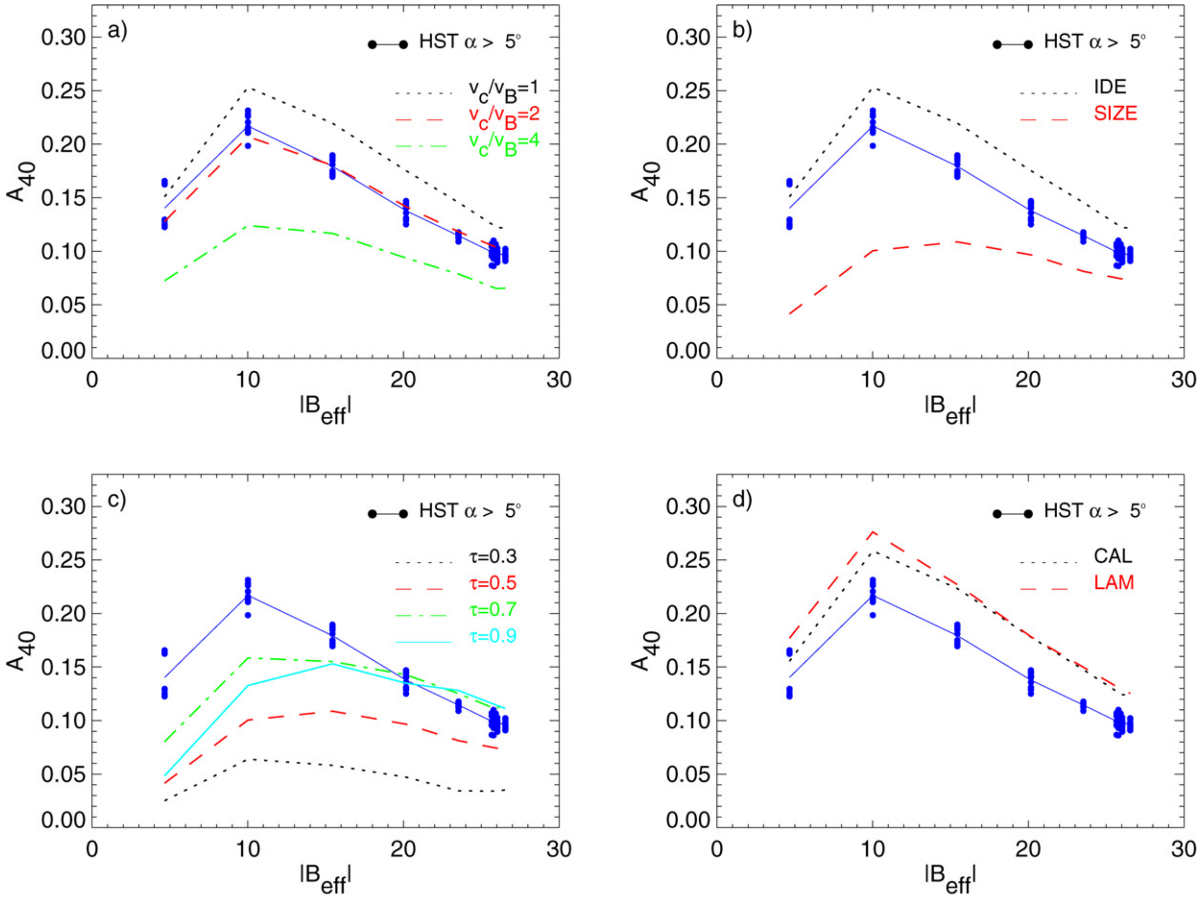

Fig. 9. The dependence of the asymmetry amplitude on various dynamical and photometric parameters. Unless otherwise indicated, the dynamical simulations have standard values $a = 130{,}000$ km, $\rho = 450\ \mathrm{kg\,m^{-3}}$, $\tau_{\mathrm{dyn}} = 0.5$, $v_c/v_B = 1$, and a Callisto phase function with $\varpi = 0.5$ is used in photometric calculations. Symbols and solid lines denote HST observations for $a = 127{,}000$–$129{,}000$ km (A128.0), limited to $\alpha > 5°$. In (a) different elasticity laws are compared for an identical particle model, (b) compares the standard IDE and SIZE models, and (c) shows SIZE models differing in their optical depth and surface density. In (d) both model curves are for the standard IDE model, but the dashed line is for a Lambert phase function with $\varpi = 0.7$.

observations extremely well for all five measures of amplitude. Expressed differently, the shapes of the model profiles nicely follow the measurements, as seen in Fig. 7. Fig. 9 summarizes the dependence of the model asymmetry amplitude on various dynamical and photometric parameters. Note that the standard IDE model with $v_c/v_B = 1$ yields about 20–25% larger asymmetry than in Fig. 8. These models assume an elasticity parameter of $v_c/v_B = 2$ (i.e., more elastic particles), resulting in slightly weaker steady state wake structure than shown in Fig. 6, and thus weaker asymmetry.

The predicted variation of the asymmetry amplitude with ring elevation also depends strongly on the assumed particle size distribution and the optical depth. Fig. 10 compares the observed and model asymmetry amplitudes for the SIZE model, with $\tau_{\mathrm{dyn}} = 0.7$. This enhanced optical depth, relative to $\tau = 0.5$ for the standard SIZE model, increases Σ by 40%, producing stronger wakes and more pronounced asymmetry, as illustrated in Fig. 9. Although the predicted magnitude is about right for large elevation, the $\tau_{\mathrm{dyn}} = 0.7$ model predicts a much more rapid decline of asymmetry for small elevations than is observed. As discussed in more detail below, the relatively large asymmetry persisting even for small B_{eff} seems to require that the interwake regions must be almost empty, as in the IDE model. In this case, the reduced brightness of the gaps produces a net brightness contrast even for very long lines of sight at low elevation angles. Overall, the IDE model provides a better match to the measurements than the SIZE model.

4.3. *Wavelength dependence of the asymmetry amplitude*

Ground-based observations have indicated that the asymmetry amplitude may be wavelength-dependent (Lumme et al., 1977; Thompson et al., 1981). Our spatially-resolved, precise photometric observations indicate that any such effect is quite small. Fig. 11 shows that the amplitude increases very gradually with wavelength. This is probably the result of enhanced multiple scattering with increased albedo at longer wavelengths. Salo et al. (2004) found a very similar effect in photometric models calculated for different albedos (see their Fig. 15). We have assumed a Callisto phase function with $\varpi = 0.2$–0.6 for $\lambda = 333$–814 nm (Porco et al., 2005), which gives approximately the correct magnitude of this effect, for both IDE and SIZE dynamical models. On the other hand, if a Lambert law is used in the models, the wavelength dependence is stronger than

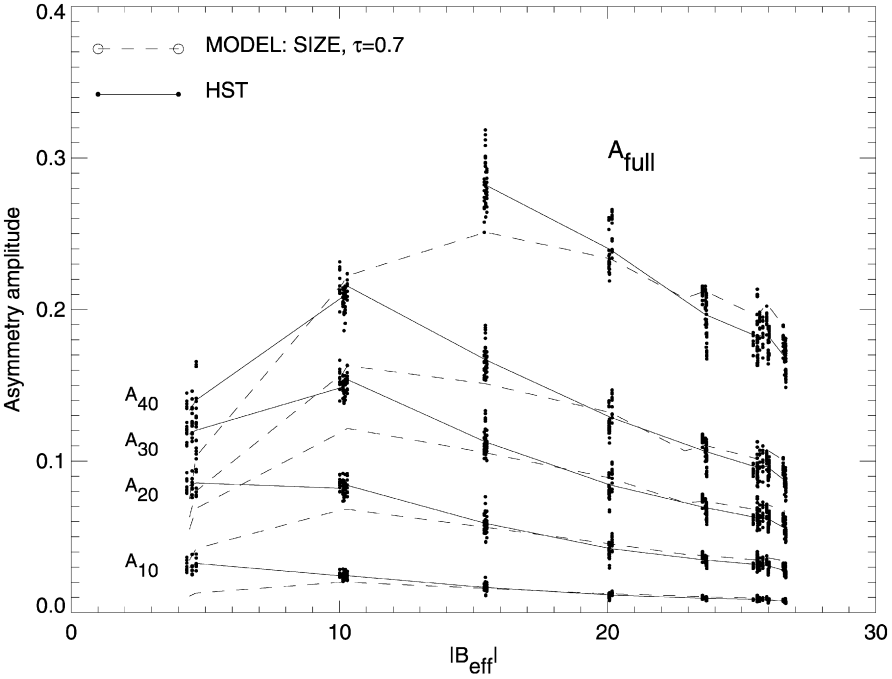

Fig. 10. Comparison of the observed and model asymmetry amplitudes for the SIZE model, with $\tau_{\rm dyn} = 0.7$. The lines and symbols have the same meaning as in Fig. 8. For clarity, only models for the mean values of each $|B_{\rm eff}|$ are shown.

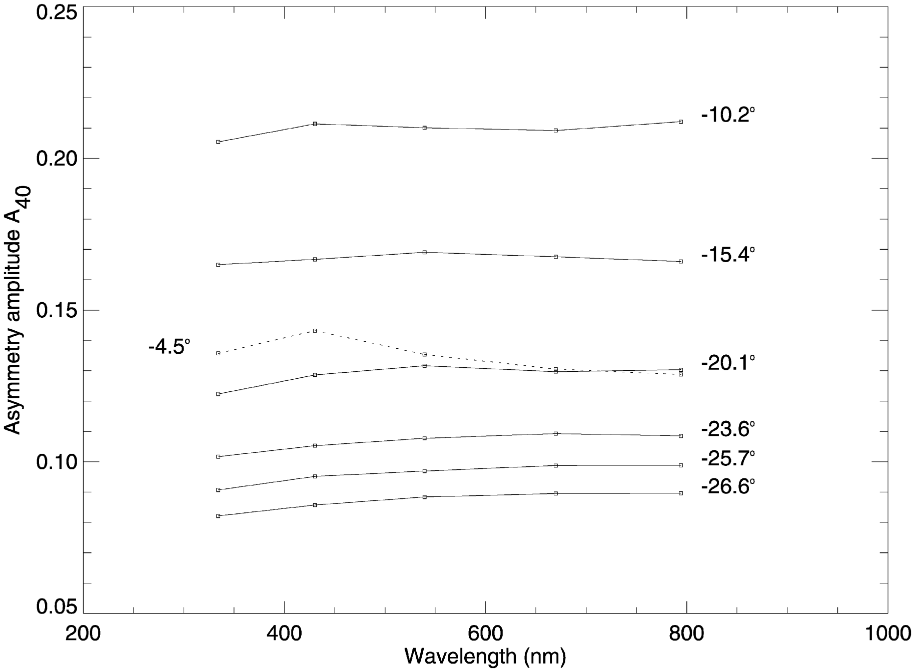

Fig. 11. Asymmetry amplitude vs wavelength for region A128.0 at different ring elevation angles $B_{\rm eff}$, as labeled.

that observed. With this less backscattering phase function, a larger ϖ is needed to account for the observed I/F levels, indicating a larger multiple scattering contribution.

4.4. Phase angle dependence of the asymmetry amplitude

Fig. 12 compares the asymmetry amplitude at A128.0 as a function of elevation angle at two phase angles ($\alpha < 1°$ and $\alpha > 5°$). The amplitude is reduced near opposition by about 5%, much less than estimated by Lumme et al. (1977) from ground-based images. Although this is a subtle effect, it is seen systematically at all elevations, even when different colors are compared separately. Both the standard IDE and SIZE models, with $\tau_{\rm dyn} = 0.5$ and $v_c/v_B = 1$, show similar shifts in amplitude for the two phase angles. Salo et al. (2004) interpreted the phase angle dependence as follows. The opposition brightening

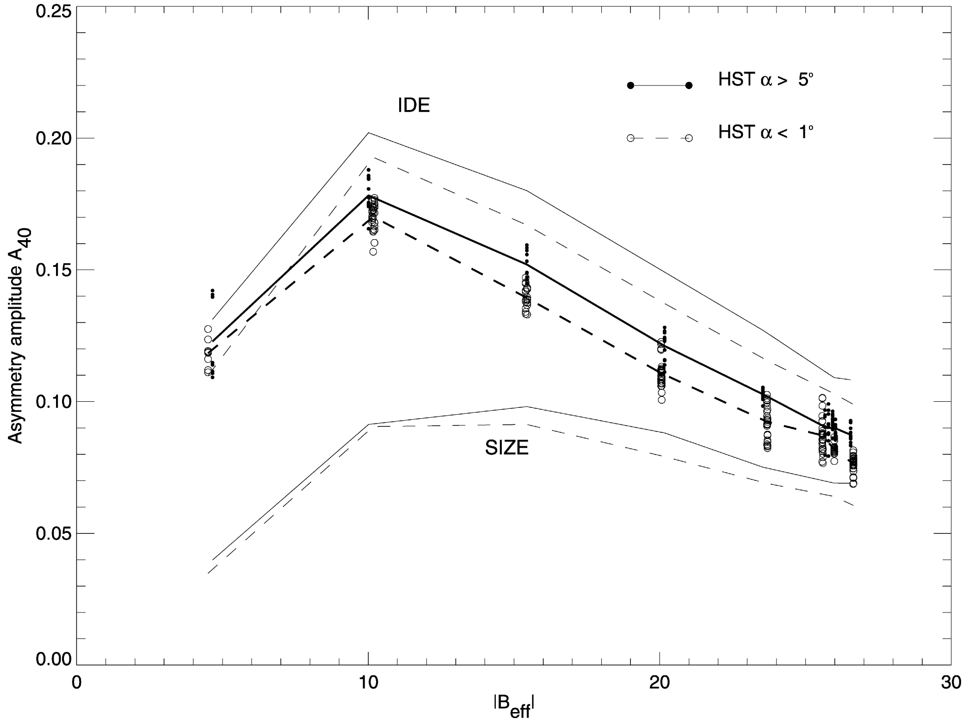

Fig. 12. Asymmetry amplitude at two phase angles. The observed A_{40} for $a = 127{,}000$–$129{,}000$ km is shown separately for $\alpha < 1°$ and $\alpha > 5°$ (all wavelengths included). Standard $\tau_{\rm dyn} = 0.5$, $v_c/v_B = 1$ IDE and SIZE models are also shown, assuming a Callisto phase function with $\varpi = 0.5$, similarly grouped according to α. Symbols and thick lines stand for observations and thin lines for models.

is stronger when viewed along the wakes than in the transverse direction, because of the long slant path optical depth in this geometry (see Salo and Karjalainen, 2003). Since the ring brightness is at a minimum along the wakes, the amplitude of the variations is reduced when the opposition effect increases. This interpretation in terms of opposition brightening, which is essentially a single-scattering effect, is supported by the fact that a similar shift is seen at all wavelengths, independent of particle albedo. The very weak contribution expected from multiple scattering is also illustrated in Fig. 9d, which shows little difference between the photometric models using the Callisto phase function with $\varpi = 0.5$ and a Lambert phase function with $\varpi = 0.7$.

4.5. Longitude of brightness minimum

As discussed in detail in Salo et al. (2004), our dynamical and photometric models predict that the longitude of minimum brightness depends on the illumination and viewing geometry. For small phase angles, the brightness minimum falls midway between the illumination direction and the long axis of the wakes. For a wake pitch angle $\phi_{\rm wake}$ (the difference between the average wake major axis and the local tangential direction, positive in the trailing direction), the expected brightness minima thus occur at ring longitudes $\theta = 90° - \phi_{\rm wake} + \frac{1}{2}\Delta\lambda_\odot$ and $\theta = 270° - \phi_{\rm wake} + \frac{1}{2}\Delta\lambda_\odot$, corresponding to $\Delta\theta_{\rm min} = -\phi_{\rm wake} + \frac{1}{2}\Delta\lambda_\odot$, where $\Delta\theta_{\rm min}$ is the longitude of minimum brightness relative to the west or east ansa ($\theta = 90°$ or $270°$, respectively) and $\Delta\lambda_\odot$ is the longitude of subsolar point with respect to the subobserver point.[6] The modeled minimum also moves away from the ansa with increased $|B_{\rm eff}|$, when the inner portions of the wakes, with larger pitch angles, become more visible (the effective $\phi_{\rm wake}$ is increased). Salo et al. (2004) showed that the predicted longitude minimum with respect to viewing and illumination is consistent with low phase angle ($\alpha = 13°$ and $24°$) Voyager observations analyzed in Dones et al. (1993). However, because the elevation angle range was limited ($B = 13 - 16°$; $B' = 8.0°$), its effect on $\Delta\theta_{\rm min}$ was unclear. The early ground-based observations, although spanning a larger range of ring tilts, were much too noisy to reveal any reliable trends of $\Delta\theta_{\rm min}$ with $|B_{\rm eff}|$.

The present HST data, with good coverage in elevation and phase angles, and excellent photometric accuracy, now enable us to determine the dependence of the longitude of brightness minimum on both $B_{\rm eff}$ and $\Delta\lambda_\odot$. Fig. 13 illustrates the effect of $\Delta\lambda_\odot$ on $\Delta\theta_{\rm min}$ for a fixed $B_{\rm eff}$. The influence of $B_{\rm eff}$ is also evident in Fig. 7, where the minimum for the larger elevation is about 5° further away from the ansa than for the smaller $|B_{\rm eff}|$ for roughly the same $\Delta\lambda_\odot$.

An attempt to disentangle the effects of $\Delta\lambda_\odot$ and $B_{\rm eff}$ on $\Delta\theta_{\rm min}$ is illustrated in Fig. 14. The HST observations for the peak asymmetry region in the A ring have been grouped ac-

---

[6] In Salo et al. (2004), the difference in illumination and viewing was defined as $\Delta\theta_s \equiv -\Delta\lambda_\odot$, where $\Delta\theta_s = \theta_s - \theta$ is the difference between the ring longitudes counted from the subsolar and subobserver points. This was used in order to have similar notation with Dones et al. (1993). With the current definition, $\Delta\lambda_\odot$ changes from a negative to a positive value during an opposition.

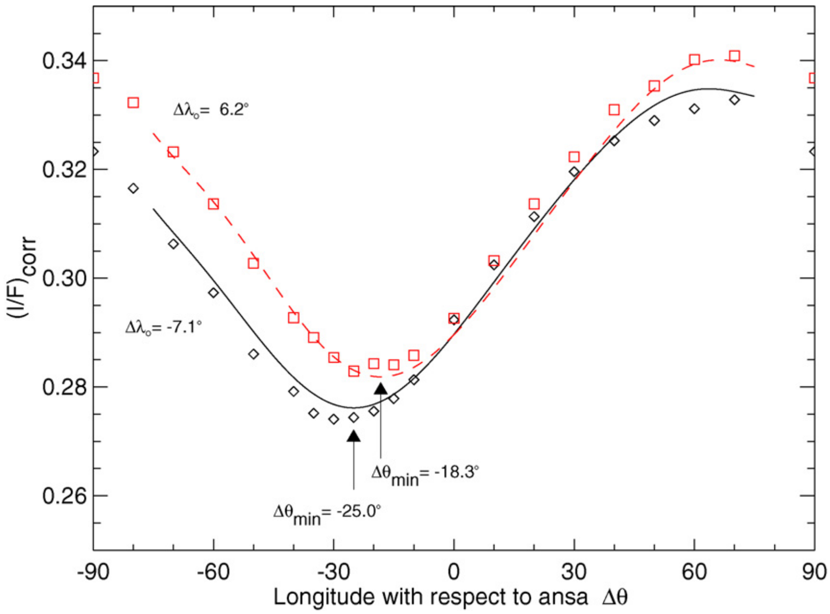

Fig. 13. Illustration of the shift in the longitude of minimum brightness with the solar longitude $\Delta\lambda_\odot$. The solid and dashed lines are HST observations in the F555W filter for $|B_{\rm eff}| = 26°$, with $\Delta\lambda_\odot = -7.1°$ and $+6.2°$, respectively. Symbols denote photometric models for the same geometries (standard SIZE model, except with $\tau_{\rm dyn} = 0.7$).

cording to $|B_{\rm eff}|$, and for each elevation, a linear fit of the form

$$\Delta\theta_{\rm min} = k_0 + k_1 \times \Delta\lambda_\odot \tag{13}$$

is shown. Fig. 15 summarizes these results. The slope, k_1, is always close to $\frac{1}{2}$, which equally weights the effects of the observer's longitude and the solar longitude. The observed scatter with $|B_{\rm eff}|$ is probably due to uneven sampling of $\Delta\lambda_\odot$ with respect to zero, varying from elevation to elevation. Although the slope is roughly constant, there is a clear systematic variation in the zero point $k_0 \equiv \Delta\theta_{\rm min}$ with $|B_{\rm eff}|$. In these figures, the results for all five filters are combined, since we found no color dependence of $\Delta\theta_{\rm min}$ or on k_1. Also shown in Fig. 15 are the results for our standard A ring models. Except for a constant shift in $\Delta\theta_{\rm min}$—IDE and SIZE models place $\Delta\theta_{\rm min}$ systematically about 1° and 7° further away from the ansa than observed—the observed trends are remarkably well reproduced. (Again, the IDE model gives the better fit.) Note that the deviations of k_1 from $\frac{1}{2}$ are also accurately reproduced. Additional models with $\Delta\lambda_\odot$ having values symmetrically around zero yield $k_1 \approx \frac{1}{2}$ regardless of $|B_{\rm eff}|$.

In Section 5, we will examine the location of $\Delta\theta_{\rm min}$ in ring regions where the azimuthal variations are much weaker than in the mid-A ring. For this purpose, it is useful to combine images at different $\Delta\lambda_\odot$, using the solar longitude correction implied by Eq. (13). Fig. 16 illustrates the effect of this correction. The upper panel shows minimum locations in the region A128.0 for all images in different filters, phase angles, and elevations, as a function of $\Delta\lambda_\odot$, while in the middle panel we have eliminated the $\Delta\theta_{\rm min}(|B_{\rm eff}|)$ derived in Fig. 15, and finally in the bottom panel we have applied the additional correction $\frac{1}{2}\Delta\lambda_\odot$, leaving just a small scatter with a standard deviation of the residuals of just 1.3°. There appears to be no systematic color dependence of the longitude of minimum brightness. Formally, the mean residuals (and standard error of the mean) in longitude are $-0.58° \pm 0.22°$ in F333W and $0.49° \pm 0.13°$ in F439W, the two filters representing the extreme values. For comparison, the original $\Delta\theta_{\rm min}$, uncorrected for the solar longitude variations, has maximum deviations amounting to nearly 10°.

4.6. *Width of the asymmetry minimum*

From the previous examples it is clear that the observed asymmetry minimum widens with increased ring opening angle (see Fig. 7). In order to quantify this effect, Fig. 17 displays the half-width-half-maximum (HWHM) of the intensity scans, measured from the minimum in the direction of elongation, where the images have the highest radial resolution. The solid line shows a second-order polynomial fit,

$$\mathrm{HWHM} = 12.8° + 125° \times |\sin B_{\rm eff}| - 132° \times |\sin B_{\rm eff}|^2. \tag{14}$$

The results from the standard IDE model, shown as a dashed line, are in good agreement with observations; other models give nearly identical results. The reduced width of the minimum as $B_{\rm eff} \to 0°$ has a clear geometrical explanation: the wakes must be viewed more and more precisely along their long axis for the gaps to become visible and thus reduce the observed brightness.

4.7. *IDE and SIZE models*

Figs. 18 and 19 provide a global comparison of the "best" IDE and SIZE models (see Figs. 8 and 10) and the observed A128.0 asymmetry over the full suite of phase angle and ring tilts in the HST data. The cases are arranged in the order of phase angle (α decreases from the left to the right) and elevation angle ($|B_{\rm eff}|$ increases from top to bottom). The particle

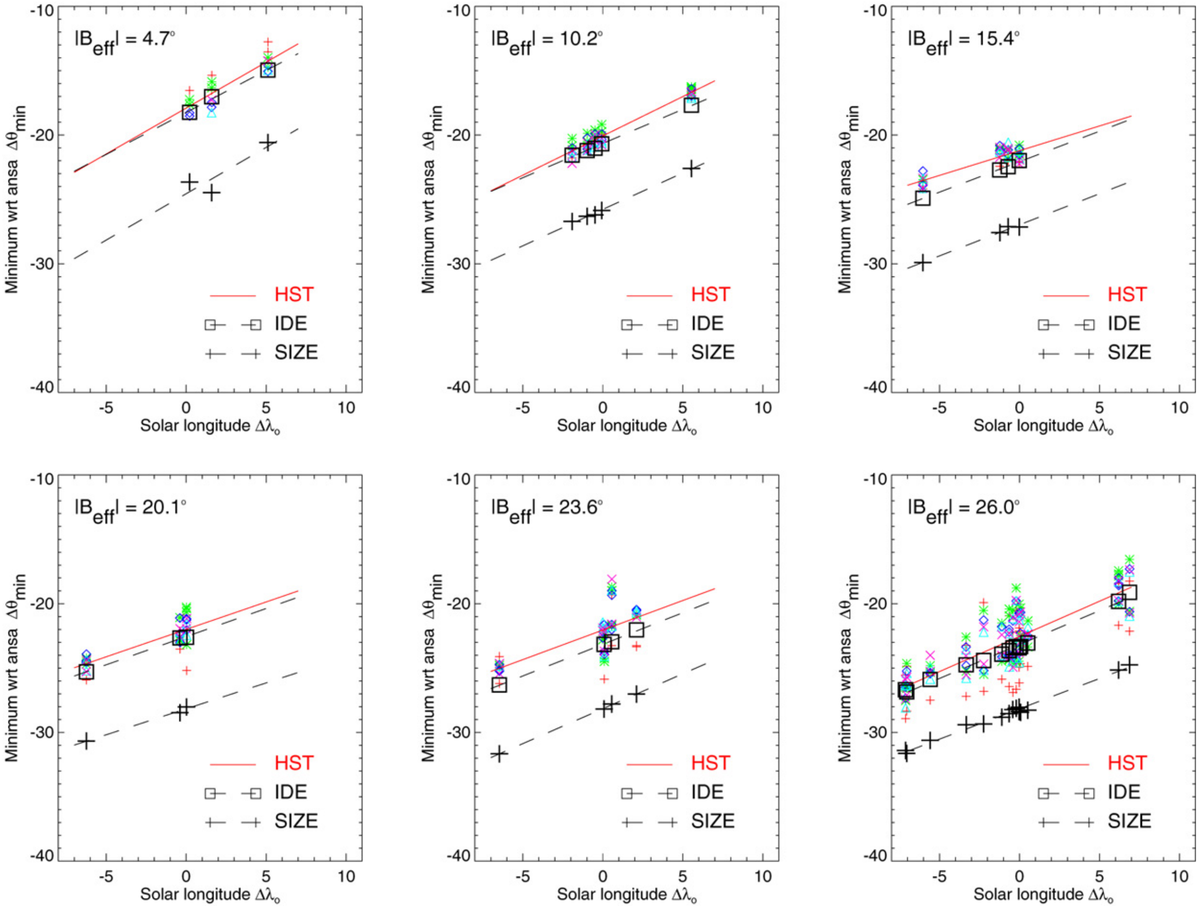

Fig. 14. The longitude of minimum brightness $\Delta\theta_{\min}$ as a function of solar longitude $\Delta\lambda_{\odot}$ for six elevation angles $|B_{\rm eff}|$. HST observations are shown as small symbols (defined in Fig. 16), overplotted with the best linear fit. Results for the standard IDE and SIZE models are shown, for the same geometries.

albedo was chosen to match the observed brightness at large α and large $|B_{\rm eff}|$. The opposition effect is seen as a mean I/F level rising from left to right, and the decrease in overall A ring brightness with increasing ring opening angle (the negative tilt effect; see Cuzzi et al., 2002; Salo et al., 2004) results in a reduction of a mean level of I/F from top to bottom. The observed trends are qualitatively reproduced by both models, as are the shapes and amplitudes of the asymmetry profiles, though neither model reproduces the strong opposition surge at low phase angle. This is not surprising, because no account has been taken of a possible intrinsic opposition effect, such as coherent backscatter by the regolith of individual ring particles, and Salo and Karjalainen (2003) showed that the particle size distribution must span at least two decades in radius in order to yield the observed magnitude of opposition brightening if interparticle shadowing alone is responsible. The match is better for the SIZE model than for the IDE model, as expected if mutual shadowing is partially responsible for the opposition effect. Finally, whereas the opposition effect is too weak in both models, the negative tilt effect is too strong. This also argues for a broader size distribution than those adopted in the simulations, which span at most one decade in radius. An enhanced small particle population would have the effect of filling in some of the gaps between wakes and weakening the observed negative tilt effect.

5. Radial variation of the asymmetry amplitude

5.1. Observations

Having compared the full range of observed asymmetry profiles in the mid-A ring with our two standard simulations, we now examine the radial variation of the asymmetry amplitude itself. Fig. 20 shows the observed A_{40} amplitude and longitude of minimum as a function of radius. In this case, the longitude scans for each distance (averaged over 500 km) were first corrected for $\Delta\lambda_{\odot} = 0°$ using Eq. (13) with $k_1 = \frac{1}{2}$, and then grouped together according to $|B_{\rm eff}|$ and averaged over all phase angles and filters.[7] The thick black crosses in the A ring region mark the wake orientation estimated by Colwell et al. (2006) from Cassini UVIS occultation studies (note that their pitch angle $\phi_{\rm wake}$ corresponds to $90° - \phi_{\rm wake}$ in our notation). Their determination was based on the direction where the path optical depth is a minimum, which according to Salo et al. (2004) simulations is identical to the longitude of minimum brightness for $\Delta\lambda_{\odot} = 0°$. The good agreement between Cassini and HST results is very encouraging.

---

[7] Here, we use A_{40} as a measure of the amplitude, in preference to the amplitude $A_{\pm\Delta\theta_{\rm range}}$ used in Figs. 4 and 5.

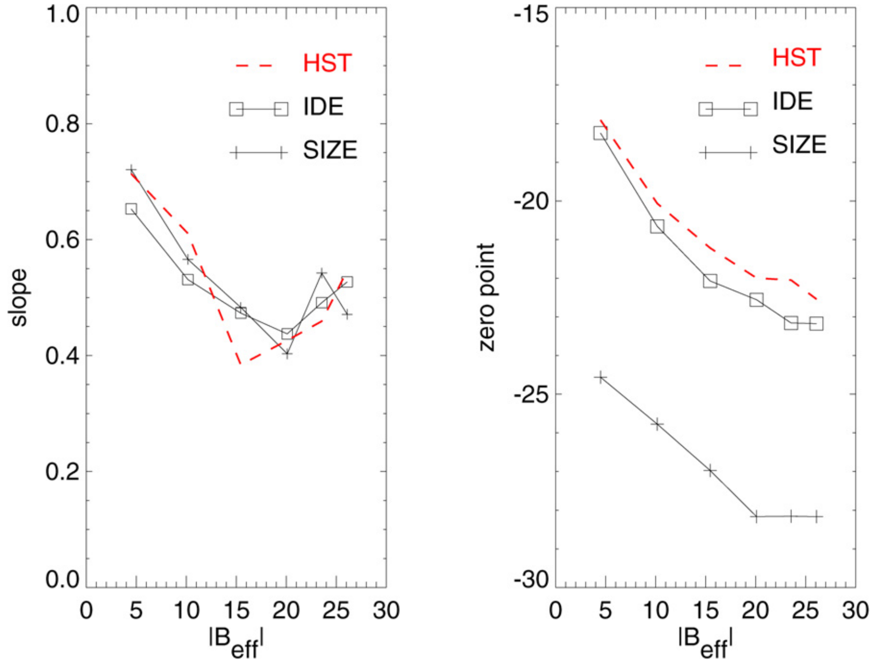

Fig. 15. Corrections for solar longitude to the predicted longitude of minimum brightness from the linear fits shown in Fig. 14. The slope (left panel) determines the relative shift of the minimum with respect to $\Delta\lambda_\odot$, and the zero point (right panel) gives the fitted longitude of minimum for $\Delta\lambda_\odot = 0°$.

5.1.1. A ring

The azimuthal asymmetry is strong throughout the A ring, as seen in Fig. 20, but there are interesting regional trends, as illustrated in more detail in Fig. 21. In the upper panel, we display the radial variation of the asymmetry amplitude A_{30} averaged over all observations at $|B_{\rm eff}| = 10°$, a ring tilt where the amplitude nears its peak (see Fig. 8), and amplitude A_{35} at a larger opening angle $|B_{\rm eff}| = 27°$ where the rings are well-resolved in longitude but where the asymmetry is weaker. The longitude of minimum brightness, corrected for solar longitude, is shown in the middle panel, and the bottom panel shows the PPS optical depth profile and a representative F555W I/F radial profile along the ansa. Three strong inner Lindblad resonances (ILR), where density waves are excited, are marked by vertical dashed lines: Janus 4:3, Janus 5:4, and Mimas 5:3. (The Mimas 5:3 bending wave excited at the inner vertical resonance, lying just inside the Mimas 5:3 ILR, is also prominent in the PPS profile.)

The asymmetry amplitude rises gradually with increasing radius, reaching a maximum near $a = 130{,}000$ km. It then decreases gradually, modulated by local reductions in amplitude in the vicinity of the Janus 5:4 and Mimas 5:3 ILRs. These are seen a bit more clearly in the $|B_{\rm eff}| = 27°$ results, which are less affected by foreshortening of the rings in the images than the $|B_{\rm eff}| = 10°$ profile. The Janus 4:3 ILR does not appear to have an effect on its regional asymmetry amplitude, although this may be masked by resolution-limited smearing by the nearby Cassini Division just interior to the resonance. The longitude of minimum brightness also shows regional trends with radius and with tilt angle. On average, $\Delta\theta_{\rm min}$ is ∼2° further from the ansa for $|B_{\rm eff}| = 27°$ than for $|B_{\rm eff}| = 10°$, echoing trends seen in Figs. 7, 14, and 15. Once again, the Janus 5:4 and Mimas 5:3 ILRs seem to affect the details of the azimuthal asymmetry, in this case by shifting $\Delta\theta_{\rm min}$ further from the ansa in their vicinities. The Janus 6:5 ILR, at $a = 134{,}300$ km, is too close to the Encke division for reliable measurements in HST images.

Both the decrease in amplitude and the shift of $\Delta\theta_{\rm min}$ near the resonances can be attributed to enhanced dynamical activity. Resonance-induced density waves produce local crowding, and thus more frequent and energetic interparticle collisions. If these collisions result in an enhanced population of relatively small ring particles, their presence would tend to decrease the asymmetry amplitude by filling in the regions between gravity wakes. This is seen quite clearly in our simulations (Fig. 9b), where the asymmetry amplitude is much stronger for the IDE than the SIZE model. Similarly, the observed shift in $\Delta\theta_{\rm min}$ away from the ansa near the resonances is expected for a broadened particle size distribution, as seen by comparing our IDE and SIZE models (Fig. 14). The picture that emerges for the A ring is one with regional trends, such as maximum asymmetry amplitude in the middle A ring, and resonance-induced, local increases in the small particle population.

5.1.2. B ring

The B ring asymmetry is substantially weaker than that in the A ring, with strong regional variations that are correlated with the underlying ring optical depth, as seen in Fig. 4. The B ring asymmetry reaches a few percent in the B96.5 region, and here we examine the radial variations in the asymmetry at this location in more detail. Fig. 22 shows the average asymmetry amplitude A_{35} (top), $\Delta\theta_{\rm min}$ (middle), and PPS optical depth (bottom) between $a = 92{,}000$ and 100,000 km, for all observations near $|B_{\rm eff}| = 27°$. (Differences between the profiles in Fig. 4 and Fig. 22 reflect the different meanings of $A_{\pm\Delta\theta_{\rm range}}$ and A_{35}.) For comparison, we include a (nearly-featureless) I/F radial profile along the ansa ($|B_{\rm eff}| = 27°$, F555W filter) in the

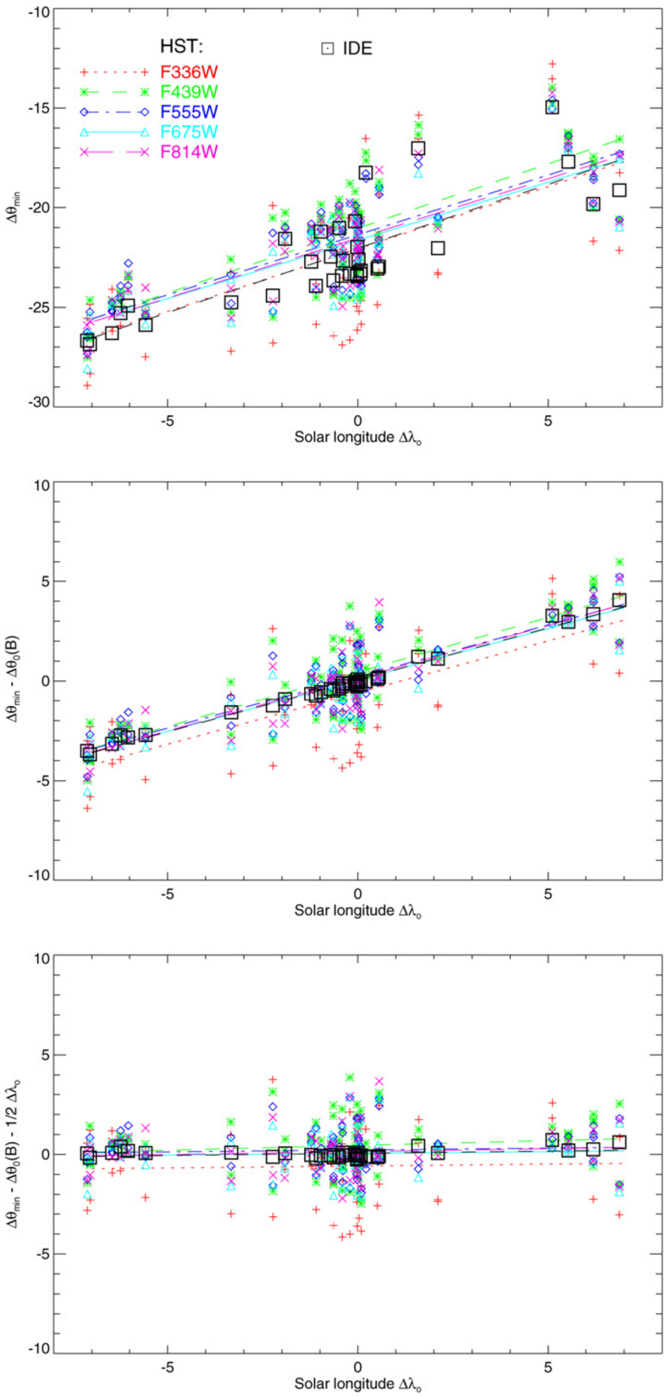

Fig. 16. Dependence of the longitude of minimum brightness on $\Delta\lambda_\odot$. In the upper panel, HST observations for all $|B_{\rm eff}|$ are shown with small symbols, together with separate linear fits for each color. In the middle panel, the elevation angle dependence is removed, while in the bottom panel, we have, in addition, applied the solar longitude correction given by Eq. (13), with $k_1 = \frac{1}{2}$. Large squares stand for the standard IDE model treated in a similar fashion as the observations.

bottom panel, plotted using the same vertical scale as the optical depth.

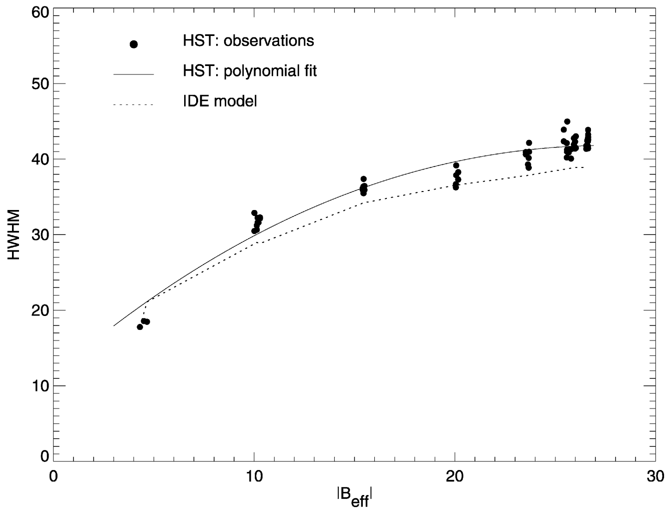

Fig. 17. Dependence of the width of the brightness minimum on the elevation angle. The width is measured in terms of HWHM, the half-width-half-maximum measured in the direction of the ansa. Symbols denote HST observations for $a = 127{,}000$–$129{,}000$ km, and the solid line is a polynomial fit according to Eq. (13). The standard IDE model results, shown as a dotted line, match the overall trend of the observations quite well.

As with the A ring, there are significant local variations in amplitude and $\Delta\theta_{\rm min}$. Two sets of vertical gray bands in Fig. 22 identify regions where $\Delta\theta_{\rm min}$ is near the ansa: just -10° near $a = 94{,}900$ km (the well-known “flat spot” in the inner B ring) and -13° near $a = 97{,}300$ km. Elsewhere in this region, $\Delta\theta_{\rm min}$ is between -20° and -30°, not substantially different from the A ring value for this ring tilt. At these same locations, there are small but significant local peaks in the asymmetry amplitude. Note, too, that both regions have relatively low, uniform, optical depth ($\tau \sim 0.7$) compared to neighboring B ring material, where τ is both larger and more rapidly variable with radius. These regional asymmetry variations probably reflect local differences in the particle size distributions. The smooth low optical depth regions are likely to have fewer small particles because of less frequent collisions, compared to the denser adjacent regions. Our IDE and SIZE models show that a paucity of small particles enhances the asymmetry amplitude and shifts $\Delta\theta_{\rm min}$ closer to the ansa (Fig. 14).

5.1.3. *Limits on asymmetry in C ring*

The tenuous C ring, close to the glare of Saturn and delineated by many barely-resolved ringlets, is a challenging target for Earth-based investigation of azimuthal brightness variations, even with the HST. Fig. 2a shows that in the regions where the optical depth varies smoothly, any asymmetry in the C ring is evidently very weak. Our goal here is to estimate an upper limit for its magnitude. In the absence of clear asymmetry, we adopted a simple scheme of measuring the difference between the ring brightness in the leading and trailing quadrants near $a = 81{,}500$ km, where the overall optical depth and I/F profiles are both relatively smooth. We estimated the average $A_{\pm\Delta\theta_{\rm range}}$ in region C81.5 (see Table 2) for the same sets of images as used for Fig. 4. Because of the proximity of Saturn’s disk to the C ring, it was essential to correct for scattered light by deconvolving the broad wings of the point spread function from each image, and to ensure that the reprojected (a, θ) images were properly registered at the level of a few tenths of

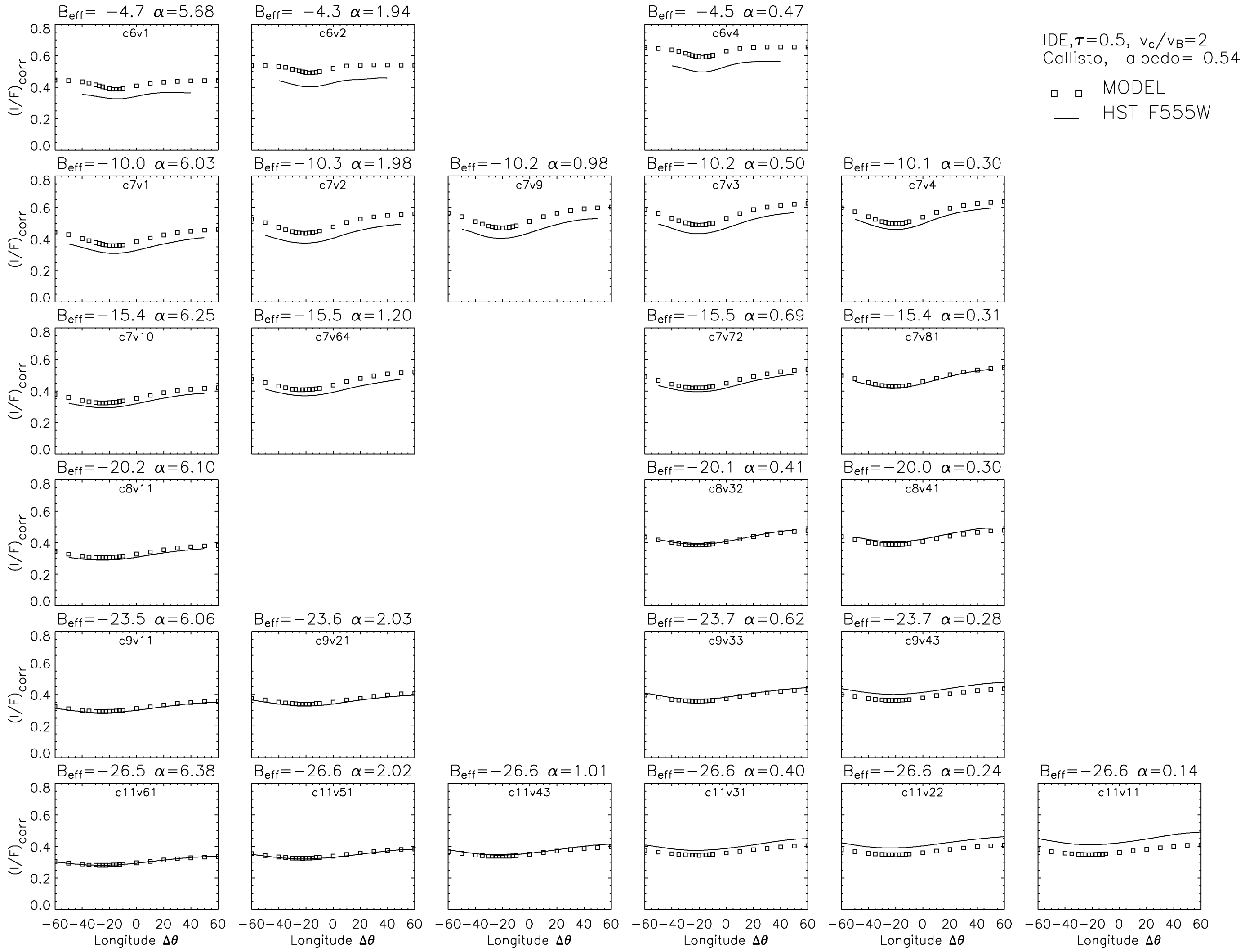

Fig. 18. Comparison of observed (solid lines) and model (symbols) azimuthal brightness scans for the A128.0 region, using the best-matching IDE model ($v_C/v_B = 2$), for a range of phase angles and ring elevations (α decreases to the right and $|B_{\text{eff}}|$ increases downward). The geometrically corrected I/F is shown. The albedo $\varpi = 0.54$ in the adopted Callisto phase function is chosen to match the I/F level of the high α, high $|B_{\text{eff}}|$ observations, at lower left. Each panel is labeled with the HST cycle and visit number (ex: c11v31is visit 31 of Cycle 11; see Table 1 and http://www.stsci.edu/hst/scheduling/program_information for details of the visits).

a pixel. We detected no compelling pattern of brightness asymmetry with ring opening angle or with radial location in the C ring, but for $|B_{\text{eff}}| = 10°$, a ring tilt at which both the A and B ring asymmetries was near their strongest, we measured a marginal asymmetry $A_{\pm\Delta\theta_{\text{range}}} \sim 0.5\%$. This is at the level of the accuracy of the measurement, and it is best regarded as an approximate upper limit. If the C ring asymmetry in C81.5 were as large as that seen in the B ring in regions B96.5 (3%) or B102.5 (1%) (see Fig. 4), it would have been readily detectable. Below, we explore possible explanations for such a weak or non-existent asymmetry in the C ring.

5.2. *Models for the main ring regions*

How can we account for the dramatic variations in the strength of the asymmetry with orbital radius shown in Fig. 20? The tendency of wakes to form clumps—as opposed to the ring material aggregating entirely into clumps—represents a competition between the mutual self-gravity of ring particles and the planet's tidal shear. For fixed particle properties such as internal density and dynamical optical depth, the transient wakes get stronger and stronger with distance from the planet, until they eventually start to collapse into semi-permanent particle aggregates (Salo, 1992, 1995; Karjalainen and Salo, 2004). In this sense, the occurrence of strong asymmetry in the outer parts of the ring system is not surprising. However, the reduction in shear is rather gradual, which by itself would result in a correspondingly gradual variation in asymmetry amplitude, as illustrated in Fig. 23. The results are shown for dynamical simulations similar to our standard $\tau_{\text{dyn}} = 0.5$ IDE model, except for different Saturnocentric distances and internal particle densities; the photometric models are for $B = B' = 10°$, $\alpha = 0°$. For comparison, the amplitudes from HST and Voyager observations at the same B_{eff} are also shown.

The asymmetry amplitude initially increases with orbital radius as a result of the increased density contrast between the

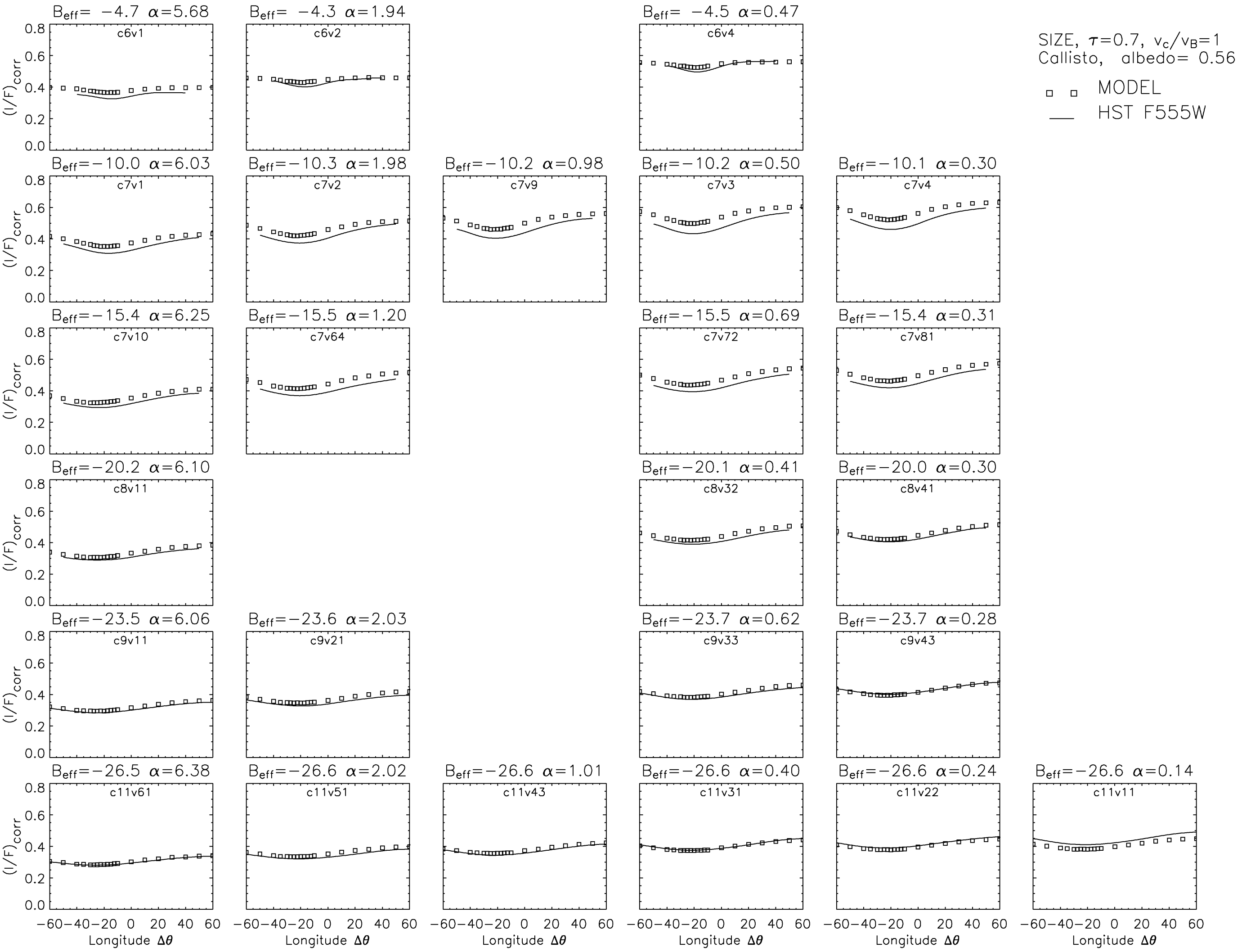

Fig. 19. Same as Fig. 18, except for the best-matching SIZE model ($\tau_{\rm dyn} = 0.7$) and $\varpi = 0.56$.

wake and interwake regions, eventually decreasing because of the pronounced clumpiness of the wakes. Even though the density contrast of the wakes is still large, the associated brightness asymmetry is diminished by the increasingly disordered wake orientations (see Fig. 1 in Karjalainen and Salo, 2004). The radial location of the maximum asymmetry amplitude depends primarily on the internal density of particles: for our standard value $\rho = 450\ \mathrm{kg\,m^{-3}}$, this is located close to the observed peak near $a = 130{,}000$ km. For other internal densities, the location varies as $a \propto \rho^{-1/3}$ from the requirement that the ratio between each particle's Hill sphere radius and its physical radius remains unchanged. For example, if the ring particles had the density of solid ice, $\rho = 900\ \mathrm{kg\,m^{-3}}$, the modeled peak asymmetry amplitude would occur in the mid-B ring, and would fall off sharply from the inner to the outer A ring, contrary to the observations. As we have discussed, the amplitude of the brightness asymmetry depends on several dynamical parameters ($\tau_{\rm dyn}$, ϵ_n, size distribution; see Fig. 9), as well as the internal density of the particles. However, changing these parameters affects the asymmetry amplitude in a roughly similar manner at all distances. Thus, the shape of the amplitude vs distance curve would not be qualitatively different from the models shown, even if other constant parameters were adopted.

The ring system is clearly much more regionally variable than implied by the above simple set of models, which assumed fixed dynamical parameters. Most notably, the simulated asymmetry maximum is very broad, not at all like the strong observed peak of the asymmetry amplitude in the mid-A ring. The current HST observations are in remarkably good agreement with the asymmetry profile derived from Voyager images (Dones et al., 1993). Both measurements suggest that the strength of the wakes varies quite strongly with radial location in the rings due to regional differences in the ring particle properties. For example, the particles might become more inelastic with increased distance due to a larger amount of surface regolith, or the particle size distribution might be more heavily truncated. Such changes might help to explain the steep rise of the amplitude in the inner and middle A ring. Another striking difference between the $\tau_{\rm dyn} = 0.5$ models and observations is the absence of measurable asymmetry in most of the B ring, except for its inner parts. The magnitude of inner B ring asym-

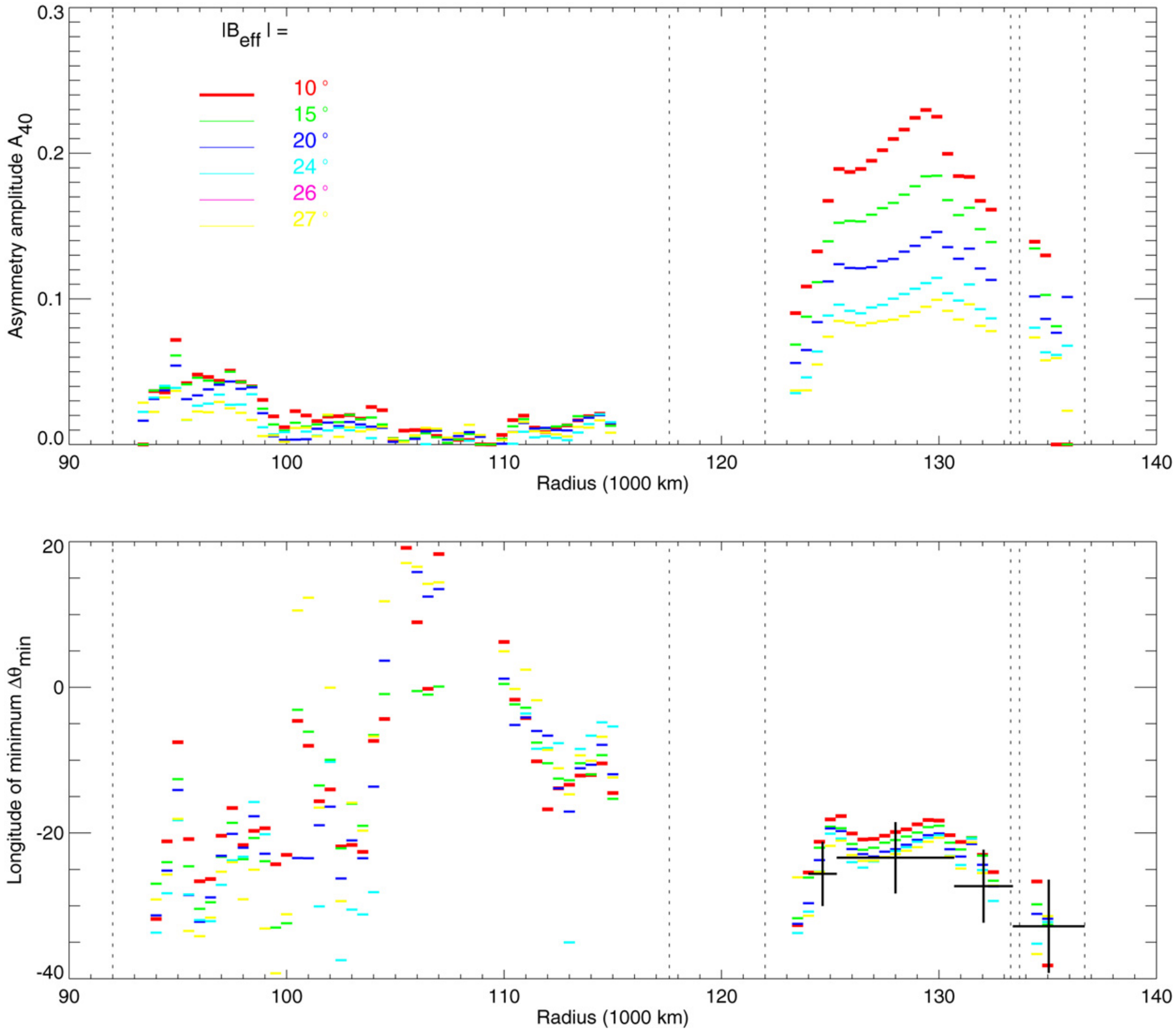

Fig. 20. The observed asymmetry amplitude A_{40} and longitude of minimum brightness, corrected for solar longitude, as a function of ring orbital radius in the A and B rings, for several ring elevations. For each HST image, azimuthal brightness scans were averaged over 500 km wide radial bins. Each plotted point represents the average for all images in each labeled ring elevation group. For clarity, $|B_{\mathrm{eff}}| = 4.5°$ scans are omitted. The vertical dashed lines denote boundaries between the main ring regions. Also shown are the results from Cassini UVIS occultations (Colwell et al., 2006), marked by crosses. The horizontal length of each cross corresponds to the radial interval of each measurement, and the vertical extent to their estimated range of uncertainty of the pitch angle.

metry amplitude itself seems to be consistent with the modeled A ring asymmetry. For example, the $\rho = 450\ \mathrm{kg\,m^{-3}}$ model curve gives the right order of magnitude for the maximum A and inner B ring asymmetries, allowing for the larger τ of the inner B ring.

Compared to the A ring and the inner B ring, the asymmetry estimates from observations of the mid- and outer B ring are much less certain. Here, the asymmetry amplitude derived from HST observations is nearly zero and the longitude of minimum seems to be shifted toward the ansa. Because of the high optical depth, strong dynamical wakes would be expected at these locations, provided that the surface mass density scales with the optical depth. This would be the case if the size distribution and internal density of particles were similar to those in the inner B ring and A ring. An intriguing possibility is that the gravity wakes are superimposed upon, or even suppressed by, a viscous overstability, manifested as spontaneous axisymmetric oscillations described previously in Section 3.2[8] (see the B ring $\tau = 1.5$ IDE model in Fig. 6). The IDE model in Fig. 6 was deliberately chosen to illustrate the overstable oscillations. However, it is worth noting that the model is quite close to the threshold of overstability. For example, replacing the IDE model with the presumably more realistic $\tau_{\mathrm{dyn}} = 1.5$ SIZE model would stabilize the simulated ring, leading to a gravity wake-dominated system with normal asymmetry behavior, except having ~70% larger amplitude than in the inner B ring $\tau_{\mathrm{dyn}} = 0.7$ SIZE model. Nevertheless, the simulations in Salo et al. (2001) suggest that overstability would probably still take place if the optical depth were further increased, or if the particles were made more inelastic (such as with constant ϵ_n close to zero). Reducing the strength of self-gravity would also

---

[8] These features may produce distinctive signatures in the azimuthal brightness profile of the B ring, a possibility we leave to future investigations.

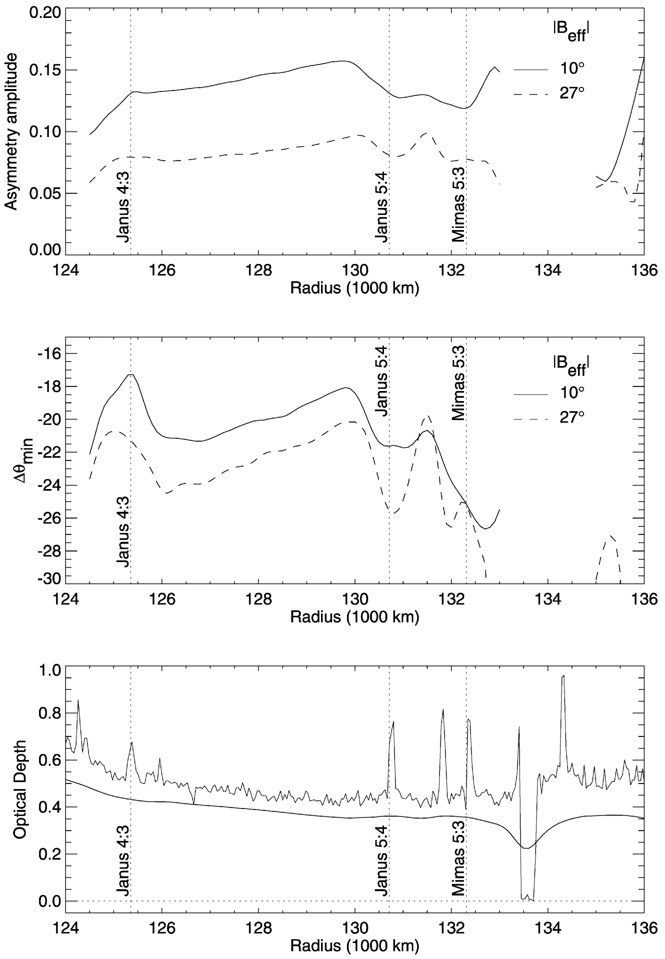

Fig. 21. The asymmetry amplitude (top) and longitude of minimum brightness (middle) of the A ring at two ring opening angles, and the PPS optical depth (bottom), as a function of radius. For $|B_{\mathrm{eff}}| = 10°$, we use A_{30}, and for $|B_{\mathrm{eff}}| = 27°$ we use A_{35}. Three strong inner Lindblad resonances (Janus 4:3, Janus 5:4, and Mimas 5:3) are marked by vertical dashed lines. For comparison, a typical I/F profile along the ansa ($|B_{\mathrm{eff}}| = 27°$, F555W filter) is shown as a bold solid line in the lower panel, plotted using the same vertical scale as the optical depth.

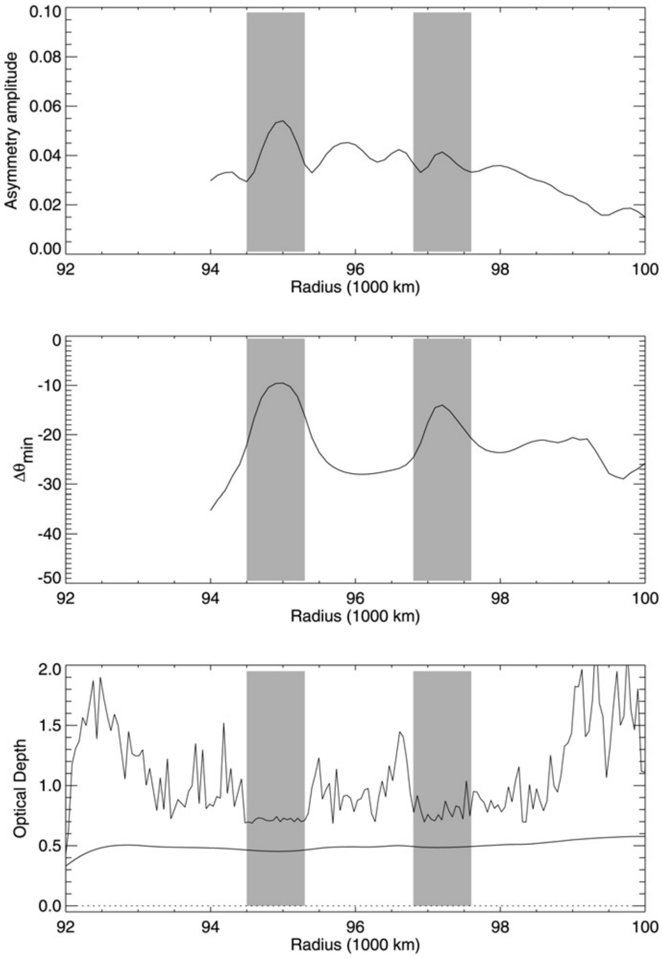

Fig. 22. The asymmetry amplitude A_{35} (top) and longitude of minimum brightness (middle) of the inner B ring, and the PPS optical depth (bottom), as a function of radius. For comparison, a typical I/F profile along the ansa ($|B_{\mathrm{eff}}| = 27°$, F555W filter) is shown as a bold solid line in the lower panel, plotted using the same vertical scale as the optical depth. The vertical gray bands mark two smooth regions of relatively low optical depth ($\tau \simeq 0.7$). At these locations, the asymmetry amplitude is slightly enhanced and the longitude of minimum brightness is shifted sharply closer to the ansa.

promote overstability. This would be the case if the increased τ_{dyn} were not accompanied by a similar increase in Σ: for example, if the changes in τ_{dyn} were mainly due to changes in the size distribution, rather than in the abundance of particles. The overstable IDE model may thus represent the potential behavior of very dense portions of the B ring (with $\tau_{\mathrm{dyn}} > 2$–3) better than the non-overstable SIZE model for $\tau_{\mathrm{dyn}} = 1.5$. Unfortunately, increasing τ_{dyn} beyond 1.5 in our particle size models is beyond our current computational resources.

The modeled asymmetry amplitude of the C ring is consistent with the observational upper limit of 0.5%, for $\rho = 450\ \mathrm{kg\,m^{-3}}$. According to Fig. 23, the amplitude for $\tau_{\mathrm{dyn}} = 0.5$ is less than about 1% for $a \leqslant 90{,}000$ km. Models using the observed value $\tau_{\mathrm{dyn}} = 0.1$ yield even smaller amplitudes, on the order of the noise limit in our simulations (about 0.3%). If the internal density of the particles were close to that of solid ice, some signs of asymmetry would be expected, at least in the dense C ring ringlets, but these are below the resolution of our HST observations.

5.2.1. Amplitude variations for selected regions

The observed dependence of the asymmetry amplitude with ring tilt is shown in Fig. 24 (upper left) for four ring regions: A128.0, A135.0, B96.5, and B113.7 (in order of decreasing maximum amplitude). Results are shown (lower left) for the four dynamical models illustrated in Fig. 6 and summarized in Table 3, selected to represent, in a rough manner, each of the ring regions. The observed asymmetry amplitude A_{40} reaches its maximum at $|B_{\mathrm{eff}}| \sim 10°$ in A128.0 and for $|B_{\mathrm{eff}}| = 10° - 15°$ in B96.5. Similar behavior is seen in the A ring IDE and the inner B ring $\tau_{\mathrm{dyn}} = 0.7$ SIZE models (Models I and III, respectively). We interpret these trends as a result of the wake geometries of the two models (see Table 3). For the A ring, the wakes are thinner than for the B ring, relative to the width of the interwake gaps ($H/S \approx 0.2$ and 0.5 for the

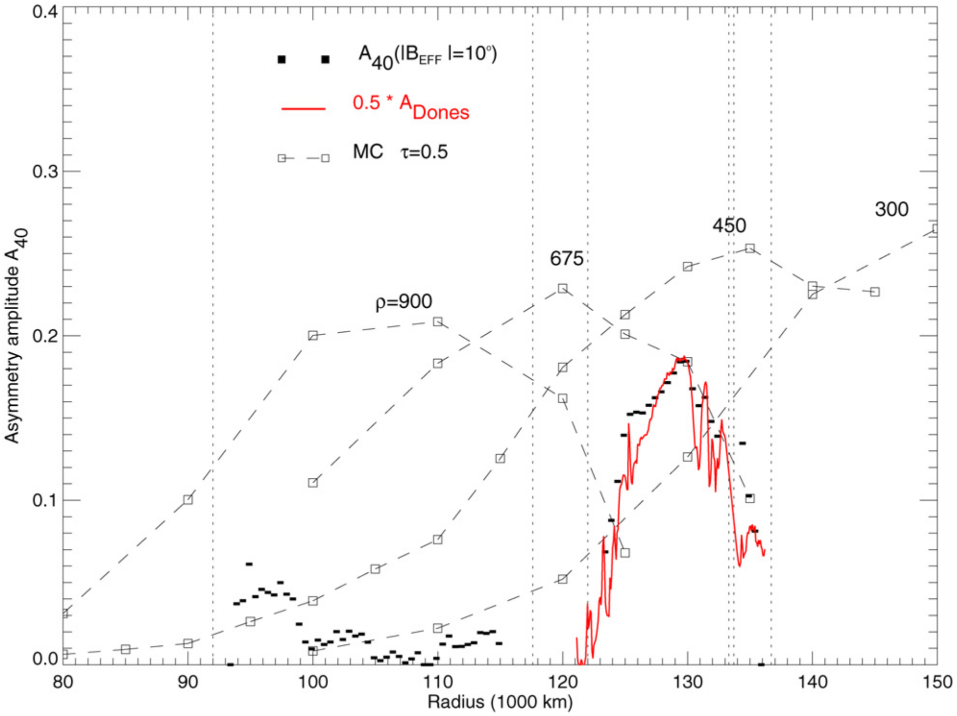

Fig. 23. The observed radial dependence of the asymmetry amplitude A_{40} is compared with dynamical simulations performed for various internal particle densities ρ as labeled, in $\mathrm{kg\,m^{-3}}$, with each open square corresponding to a Monte Carlo simulation at a given radial distance. The particle size was varied as ρ^{-1} so as to keep $\Sigma/\tau_{\mathrm{dyn}}$ constant. All simulations assumed $\tau_{\mathrm{dyn}} = 0.5$ and $v_c/v_B = 1$, just as in the standard IDE model. Both the HST observations (filled squares) and models correspond to $|B_{\mathrm{eff}}| = 10°$. The asymmetry amplitude from Voyager images at $B_{\mathrm{eff}} = 10°$ as measured by Dones et al. (1993) is also shown as a solid line, multiplied by a factor of 0.5 to account for the difference in definitions.

A and B ring models, respectively). For the relatively larger H/S of the inner B ring model, the dependence of the visibility of gaps on ring azimuth should persist to larger elevation angles. That is, the hiding of gaps by wakes continues until $\tan(B) \geqslant H/S$, after which the asymmetry amplitude should decline. This simple estimate, which assumes an opaque wake with a rectangular slab profile (similar to that in Colwell et al., 2006), suggests that maximum amplitude should occur at elevations near $|B_{\mathrm{eff}}| = 13°$ and 26°. The qualitative trend is correct, although the quantitative agreement with photometric calculations is poorer, because of the oversimplification of the opaque slab model (see Table 3).

The observed variations in asymmetry amplitude with ring tilt in the A128.0 and B96.5 regions are well-matched, both in amplitude and general trend with $|B_{\mathrm{eff}}|$, by their corresponding models (I and III, respectively). The weaker asymmetry in the B ring is a direct consequence of the smaller wake contrast: in the inner B ring SIZE model, $\tau_{\mathrm{gap}} \sim 0.3$–$0.4$, or at least 3 times that in the A ring IDE model (Table 3). The outer B ring observations (B113.7) are also matched reasonably well by the B ring $\tau_{\mathrm{dyn}} = 1.5$ IDE model. Here, the observed dependence of the asymmetry amplitude on elevation is very weak, which is also the case in Model IV. Formally, the estimated wake parameters listed in Table 3 would suggest that the maximum asymmetry amplitude would be reached at rather large elevations (26° for B96.5 and 22° for B113.7).

In the outer A ring (A135.0), the observed asymmetry amplitude is about 2/3 that in the mid-A ring (A128.0), although the trend with ring tilt is very similar in the two regions (Fig. 24). It is similar to that of our standard A ring SIZE model (Model II in the figure), suggesting that the reduced asymmetry near the A ring outer edge could reflect a more extended size distribution. Alternatively, it could result from the increased clumpiness of the wakes resulting from the weaker tidal shear. However, as discussed earlier, this latter trend is too gradual to account for the observed decrease in amplitude of almost 30%. To obtain an amplitude vs. elevation curve similar to that in Model II, the Saturnocentric distance of the standard A ring IDE model would have to be increased by nearly 25%, from 130,000 km to about 165,000 km (see Table 3). In actuality, the distances of the compared ring regions differ only by 5%.

5.2.2. *Minimum longitude variations for selected regions*

Overall, the trends in asymmetry amplitude with ring tilt for the four selected regions are well-matched by their corresponding dynamical models. We now compare how well the observed longitude of minimum brightness θ_{min} is matched by the model predictions for these regions. In Fig. 24 at right, the inner B ring and mid-A ring observations are fairly similar, showing a gradual shift of the minimum away from the ansa with increased elevation. This trend is well matched by the IDE Models I and III (see Fig. 14). In contrast, for A135.0 there is a very clear shift of the minimum towards the ansa with increased $|B|$. At some level, this is expected from the gradual degradation of wakes into clumps as the shear is reduced at larger distances. However, for a given Saturnocentric distance the clumping of wakes is always stronger for SIZE than for IDE models and there is a clear increase in the pitch angle in the centers of the

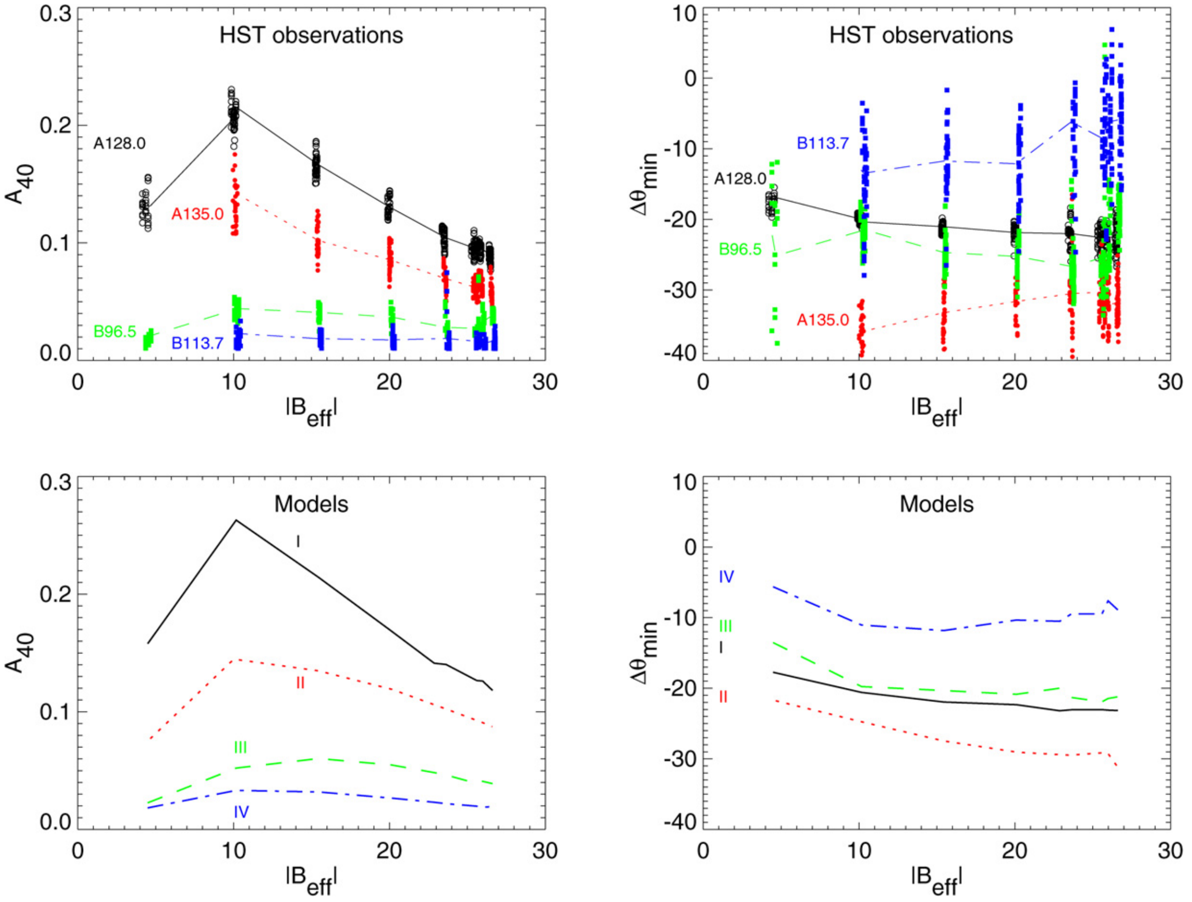

Fig. 24. Comparison of the observed asymmetry amplitude and longitude of minimum brightness with several dynamical models. Upper panels: the full set of HST observations for four radial regions in the A and B rings, including all wavelengths and phase angles. Lower panels: the asymmetry amplitude and longitude of minimum brightness from the A and B ring models shown in Fig. 6. Here, I and II stand for the standard IDE and SIZE model for the A ring, III is the $\tau_{\rm dyn} = 0.7$ SIZE model, and IV is the $\tau_{\rm dyn} = 1.5$ IDE model for the B ring.

SIZE model wakes (Salo et al., 2004). This is due to the higher maximum packing density for the case of a size distribution, which increases the effective mass density for a fixed internal particle density. The change in the outer A ring may thus be associated with a broader size distribution in this region. The standard A ring SIZE model (II), with a similar shift in the longitude of minimum and a reduction in the asymmetry amplitude, provides a good match to the outermost A ring.

In the dense B ring region (B113.7), the longitude of minimum brightness is only 10–15° from the ansa. This resembles the B ring $\tau_{\rm dyn} = 1.5$ model (IV), where a similar effect is caused by the superposition of tilted wakes and axisymmetric overstable oscillations. In the very densest part of the B ring ($a = 105{,}000$–$110{,}000$ km), the observations suggest a reversal in the sense of the asymmetry, with the longitude of minimum brightness on the leading, rather than the trailing, side of the ansa (see Figs. 4 and 20). Although this effect is just at the level of detectability (the estimated error in the asymmetry is ± 0.001), its persistence at nearly all ring tilts provides some support that it is real. We have not identified any systematic errors such as image misregistration and finite resolution, or unmodeled effects such as Saturnshine, that could cause this behavior. In the absence of a dynamical explanation, we must await additional observations to provide a clearer picture of this high optical depth region.

6. Discussion and conclusions

Using a superb long-term series of HST WFPC2 images, we have explored many intriguing characteristics of the azimuthal brightness variations in Saturn's rings. The extensive geometric coverage, high spatial resolution, and photometric precision of the observations have enabled us to measure the dependence of the asymmetry amplitude and longitude of minimum brightness on orbital radius, ring elevation, wavelength, solar phase angle, and solar longitude. Here, we summarize the observed properties of the asymmetry, describe our model results, compare these with other studies, and describe directions for future work.

The asymmetry is most prominent in the A ring, reaching a maximum just outside of A128.0, with reduced amplitude near strong Inner Lindblad resonances and outside of the Encke Division. The measured radial profile of the asymmetry amplitude from the HST data very closely matches the Voyager results (Dones et al., 1993), for the same ring opening angle. A key finding is that the B ring shows significant asymmetry, especially in regions of relatively low optical depth. In this respect, the inner B ring resembles the mid-A ring, albeit with a much weaker asymmetry (A_{40} reaches 0.05 in the B96.5 region, compared to 0.25 in A128.0). In the middle and outer B ring (B102.5 and B113.7), where $\tau \sim 1$, the asymmetry amplitude is even weaker, with a maximum amplitude of just under 1%. There is some indication of weak (0.3%) asymmetry in the optically thick ($\tau > 2$) central B ring, centered at $a = 107{,}000$ km, but it is at the margin of detectability in our data. We establish an upper limit on the C ring asymmetry of about 0.5% for $|B_{\mathrm{eff}}| = 10°$ in the quasi-uniform C81.5 region.

The A ring asymmetry amplitude varies strongly with ring elevation, reaching a peak near $|B_{\mathrm{eff}}| = 10°$, confirming earlier ground-based studies (Lumme and Irvine, 1976; Lumme and Irvine, 1979b; Thompson et al., 1981). In the inner B ring, the amplitude peaks at somewhat larger elevations of 15°–20°. There is a very slight weakening of the asymmetry at shorter wavelengths, where the albedo of the ring particles is lower and multiple-scattering effects are diminished. The wavelength effect is much weaker than had been previously estimated from ground-based measurements (Lumme et al., 1977; Thompson et al., 1981). The asymmetry also weakens very near opposition, but by less than suggested previously (Lumme et al., 1977).

The longitude of minimum brightness, typically between 20°–30° before elongation in the trailing ansa, shows distinct trends with radius, ring elevation, and solar longitude. In the inner A ring ($a = 126{,}000$–$130{,}000$ km), $\Delta\theta_{\mathrm{min}}$ moves closer to the ansa with increasing orbital distance by about 1° per 1000 km, and outside of the Encke Division, it moves sharply away from the ansa. In the inner B ring, $\Delta\theta_{\mathrm{min}}$ is similar to that in the middle A ring except in regions of comparatively low optical depth ($\tau \sim 0.7$), such as the flat spot near $a = 94{,}900$ km, where $\Delta\theta_{\mathrm{min}}$ is only 10° from the ansa. In the densest part of the B ring, there are even hints of a "reverse" asymmetry, with $\Delta\theta_{\mathrm{min}}$ leading rather than trailing the ansa. In the mid-A ring and inner B ring, the longitude of minimum brightness moves away from the ansa with increasing elevation. For the nearly backscattering geometry of our observations, $\Delta\theta_{\mathrm{min}}$ increases linearly with solar longitude; it is crucial to account for this effect when comparing observations taken under different illumination and viewing geometries.

These trends in the brightness asymmetry with orbital radius, optical depth, wavelength, and illumination and viewing geometry set very powerful constraints on the dynamical properties of the rings, as well as the physical and optical characteristics of the ring particles themselves. We have developed a suite of four dynamical and photometric models of self-gravity wakes that reproduce many of the observations. Our goal has been to explore the sensitivity of the predicted brightness variations to a range of model values, rather than to attempt to match the full set of observations in detail. In particular, we have restricted our attention to two classes of models, one with a single particle size and the second with a fixed power law distribution spanning a decade in particle radius. While our model comparisons are certainly not unique, the insights obtained from these parametric studies provide a sound point of departure for more elaborate studies in the future.

Overall, our models account quite well for many of the observed properties of the asymmetry. In the mid-A and inner B rings, where the azimuthal brightness variations are strongest, the models nicely match the shape and location of the brightness minimum, including the effects of varying ring elevation and solar longitude. We show that the asymmetry is predominantly a single-scattering phenomenon: the orientation of the illumination and observer with respect to the wakes determines the overall scattering cross-section of the rings. The relative unimportance of multiple scattering in the models is confirmed by the very weak wavelength dependence of the asymmetry amplitude.

Changes in asymmetry with ring opening angle provide an estimate of the thickness of the wakes, because gaps are hidden behind wakes of finite thickness. The longitude of minimum brightness, $\Delta\theta_{\mathrm{min}}$, also depends on ring elevation, a result of variations in the effective pitch angle of the wakes. At low ring elevation, the slant path optical depth of the rings increases and the azimuthally-varying part of the overall opacity is dominated by the optically thinner outer parts of wakes, which have an asymptotic pitch angle of about 15° (see Salo et al., 2004). The particle size distribution also affects $\Delta\theta_{\mathrm{min}}$: the pitch angle of the wakes is larger for an extended size distribution, because the central parts of the wakes are "rounder" due to the higher maximum packing density.

From our model results, the orbital radius of maximum asymmetry depends primarily on the internal density of the particles. The observed peak near A128.0 favors an internal density around 450 kg m^{-3}, although this varies slightly with the assumed elasticity and size distribution. This value also gives a good match to the observed asymmetry amplitude in the inner B ring, and is consistent with the absence of any observed asymmetry in the C ring. The regional variations in the A ring asymmetry probably reflect underlying differences in particle properties. For example, the very large peak asymmetry amplitude near A128.0 requires a rather narrow size distribution, because an abundance of relatively small particles would otherwise mute the contrast between the wakes and the gaps. We propose that the steep decline in amplitude in the inner A ring is associated with a broader size distribution in this region. This is consistent with the observed shift of $\Delta\theta_{\mathrm{min}}$ away from the ansa with decreasing radius in the region $a = 126{,}000$–$130{,}000$ km, although increased particle elasticity could also account for the decreased wake contrast. Similar arguments apply for the outer A ring, where the observed decrease in asymmetry amplitude and the shift in $\Delta\theta_{\mathrm{min}}$ away from the ansa can be explained as the result of either a more extended size distribution or increased clumpiness of the wakes. Alternatively, Dones et al. (1993) suggested that the satellite resonances could effectively pump up the velocity dispersion of the ring beyond the Encke gap, reducing the wake contrast. Colwell et al. (2006) argued instead that density waves are damped very close to exact resonance, so that their overall effect on the rings should be small. They attributed the weaker asymmetry in the outer A ring to a lower overall surface density in this region.

Wakes in the A ring are revealed not only by azimuthal variations of scattered sunlight, but also in the asymmetry of Saturn's microwave thermal radiation transmitted through the rings (Dunn et al., 2004, 2005; Molnar et al., 1999). Wake structure may also be responsible for an apparent east–west asymmetry in Saturn's thermal radiation scattered by the rings (van der Tak et al., 1999; Dunn et al., 2002). Recently, Molnar et al. (2004) have reported a similar VLA microwave asymmetry signature in the inner B ring as well. Strong asymmetry is also evident in 12.6 cm Arecibo radar observations (Nicholson et al., 2005a). A four-year series of observations near opposition at moderate ring elevation ($20.1^\circ < |B| < 26.7^\circ$) showed a strong $m = 2$ azimuthal reflectivity variation of the A ring with average amplitude $A_{\mathrm{asym}} = 0.20$ and $\Delta\theta_{\min} = -23^\circ$. This amplitude is greater than predicted by IDE models for the observed ring tilt, and Nicholson et al. (2005a) attributed the enhanced asymmetry seen in the radar images to the forward-scattering behavior of icy ring particles at decimeter wavelengths. From models fitted to the delay-Doppler radar images, they found a weaker azimuthal asymmetry in the B ring, about 1/4 of that in the A ring, but with a similar orientation. This is reasonably consistent with our results from HST images: for $|B_{\mathrm{eff}}| = 20^\circ$, Fig. 5 shows that the ratio of the maximum observed B and A ring asymmetry amplitudes $A_{\pm\Delta\theta_{\mathrm{range}}}(\mathrm{B96.5})/A_{\pm\Delta\theta_{\mathrm{range}}}(\mathrm{A128.0}) = 0.03/0.09$, or about 1/3, a bit larger than the radar results. However, we find much weaker B ring asymmetry elsewhere, which would reduce the overall average. With additional high quality Earth-based radar measurements, it may be possible to determine whether the B ring asymmetry in radar backscatter is as regionally variable as in the optical images.

Recent Cassini spacecraft measurements have provided additional evidence for azimuthal ring optical depth variations from a variety of experiments. For example, multiple Radio Science Subsystem (RSS) occultations at several ring longitudes show substantial asymmetry in the A ring as well as weaker variations in the B ring (Marouf et al., 2006). Using the VIMS instrument, Nicholson et al. (2005b) and Hedman et al. (2007) observed a set of grazing occultations of o Ceti by the outer A ring, which showed extremely strong variations of slant path optical depth with orbital longitude, matching the expected signatures of tilted wakes. The asymmetry peaked near $a = 129{,}000$ km, consistent with our results and earlier Voyager findings (Dones et al., 1993). Using a simple physical model of the wakes as opaque infinite cylinders with elliptical cross-sections, they were able to estimate the relative widths and horizontal separations of the wakes, their orientation direction, and their approximate vertical thickness. The wake orientation was between 18° and 26°, relative to the azimuthal direction, comparable to our results. They estimated the vertical thickness of the wakes to be 9–12% of the wake wavelength, a bit smaller than our estimate of $H/\lambda \sim 1/6$ (17%) (see Table 3).

Colwell et al. (2006, 2007) estimated the shape and spacing of self-gravity wakes from a series of occultations observed with the Cassini UVIS instrument. They modeled the wakes as regularly-spaced elongated slabs with rectangular cross-sections, separated by low optical depth gaps, and estimated the orientation, dimensions, and optical depths of the wake and gaps as a function of orbital radius from fits to 13 occultation profiles that sampled a range of wake longitudes and ring opening angles. Their estimate of $\tau_{\mathrm{gap}} = 0.12$ is consistent with our range of $\tau_{\mathrm{gap}} = 0.1$–$0.2$ from our IDE and SIZE models for the HST asymmetry. Our results differ, however, for the geometry of the wakes themselves. Colwell et al. (2006) found $H/W = 0.2$ at $a = 128{,}000$, whereas we find $H/W \sim 0.7$ for both models (Table 3). Direct examination of edge-on cuts across our N-body simulations confirms that the wakes have fairly circular cross-sections. We find $H/\lambda \simeq 1/6$ (17%), nearly identical to their value of 16%, so the key discrepancy between our results is the relative widths of the wakes and the gaps. The wakes in our A ring N-body simulations are much narrower than the gaps, whereas Colwell et al. (2006) modeled the wakes as much wider structures. A possible explanation is that the idealized rectangular slab model uses a bimodal optical depth distribution, while N-body simulations have a more gradual transition between the wake and the interwake gap. This could result in systematic differences in the identification of wake edges. Alternatively, this discrepancy could represent a more fundamental difference between the occultation results and the HST measurements of reflected light asymmetries.

There are a number of ways that our models can be improved. For this study, we have not attempted to match the very strong and narrow opposition peak evident in the data at very low phase angles. This spike in brightness near opposition could result in part from the scattering properties of the regolith of individual ring particles, including coherent backscattering and shadow-hiding by small surface facets. A broad particle size distribution could also contribute to the observed effect. Thus, an important future investigation is to determine the relative importance of shadow-hiding and coherent backscatter to the observed opposition effect, making use of Monte Carlo simulations for the rings based on realistic dynamical models of wakes.

Another obvious refinement of our approach is to adjust the adopted size distribution to give the best match to regional asymmetry variations, including a self-consistent model of the opposition peak. For simplicity, we have used two simple particle size distributions for all of our models. Our results show that the asymmetry amplitude and $\Delta\theta_{\min}$ are strongly affected by an abundance of relatively small (cm-size) particles. For example, we find that the mid-A ring must have a narrow size distribution near A128.0, broadening slightly outward of this region, and being substantially broader outside of the Encke Division. Similarly, we find the inner B ring to resemble the mid-A ring particle size distribution. These inferences are quite consistent with a number of other studies of ring particle size distribution. French and Nicholson (2000) used ground-based and Voyager stellar occultation data to measure the diffracted light scattered by the ring particles. They found a rather flat and narrow size distribution for both the inner A and B ring, with a surprisingly large lower particle size cutoff of 30 cm. They also concluded that the fraction of cm-sized particles increases between the inner and outer A ring, and is greatest in the C ring. (A broad size distribution in the C ring would imply an even weaker asymmetry amplitude than our upper limit of 0.5%.) Voyager radio occultation studies showed similar results from an analysis of the differential extinction and forward-scattering cross-section of the rings (Marouf et al., 1983), and upper particle size limits have also been estimated from the statistical properties of the Voyager PPS stellar occultation (Showalter and Nicholson, 1990). The Cassini RSS ring occultation experiments should provide an even more detailed view of the particle size distributions, because for the first time they are carried out at three wavelengths ($\lambda = 12$, 3.6, and 0.9 cm) at a high signal-to-noise ratio over a range of ring opening angles (Wong and Marouf, 2004; Thomson et al., 2005; Marouf et al., 2005). Whereas French and Nicholson (2000) assumed a classical many-particle-thick radiative transfer model and considered only single-scattering, the Cassini RSS results are modeled using realistic finite-size particles whose spatial distribution is based on N-body dynamical simulations and multiple scattering. These and other independent estimates of the particle size distribution of the rings will provide useful checks for the next generation of brightness asymmetry models.

The HST observations span the full range of viewing and illumination geometries accessible from the Earth, and are particularly useful for studying ring tilt and color dependencies, as well as the abrupt brightening near opposition. However, they are limited in radial resolution and solar phase angle coverage. Cassini images should reveal whether there are highly localized variations in the asymmetry in the vicinity of density waves, as seen by Hedman et al. (2007), and additional Earth-based radar measurements at smaller opening angles should provide independent estimates of the effects of multiple scattering and ring tilt on the A and B ring asymmetry. A host of Cassini radio and stellar occultations will sharpen our view of the poorly understood dense B ring, and perhaps provide compelling evidence for viscous overstability in this region. Coupled with improved dynamical models, these promise to deepen our understanding of the physics of Saturn's rings.

Acknowledgments

We thank Phil Nicholson for helpful conversations, and for sharing Cassini VIMS results prior to publication. Tony Roman and the rest of the HST team provided outstanding support for the observations. We are grateful to Essam Marouf for discussions concerning the Voyager and Cassini RSS ring occultations. We thank Josh Colwell and Alar Toomre for rigorous and constructive reviews. Our results are based on observations with the NASA/ESA Hubble Space Telescope, obtained at the Space Telescope Science Institute (STScI), which is operated by the Association of Universities for Research in Astronomy, Inc. under NASA Contract No. NAS5-26555. This work was supported in part by STScI, by the National Science Foundation, and by NASA's Planetary Geology and Geophysics program. Support from the Academy of Finland is also acknowledged.

References

Bridges, F.G., Hatzes, A., Lin, D.N.C., 1984. Structure, stability and evolution of Saturn's rings. Nature 309, 333–335.

Camichel, H., 1958. Mesures photométriques de Saturne et de son anneau. Ann. Astrophys. 21, 231–242.

Colombo, G., Goldreich, P., Harris, A.W., 1976. Spiral structure as an explanation for the asymmetric brightness of Saturn's A ring. Nature 264, 344–345.

Colwell, J.E., Esposito, L.W., Sremčević, M., 2006. Self-gravity wakes in Saturn's A ring measured by stellar occultations from Cassini. Geophys. Res. Lett. 33, 7201.

Colwell, J.E., Esposito, L.W., Sremčević, M., McClintock, W.E., Stewart, G.R. 2007. Self-gravity wakes and radial structure of Saturn's B ring. Icarus, in press.

Cuzzi, J.N., French, R.G., Dones, L., 2002. HST multicolor (255–1042 nm) photometry of Saturn's main rings. I. Radial profiles, phase and opening angle variations, and regional spectra. Icarus 158, 199–223.

Daisaka, H., Ida, S., 1999. Spatial structure and coherent motion in dense planetary rings induced by self-gravitational instability. Earth Planets Space 51, 1195–1213.

Dones, L., Cuzzi, J.N., Showalter, M.R., 1993. Voyager photometry of Saturn's A ring. Icarus 105, 184–215.

Dones, L., Porco, C.C., 1989. Spiral density wakes in Saturn's A ring? Bull. Am. Astron. Soc. 21, 929.

Dunn, D.E., Molnar, L.A., Fix, J.D., 2002. More microwave observations of Saturn: Modeling the ring with a Monte Carlo radiative transfer code. Icarus 160, 132–160.

Dunn, D.E., Molnar, L.A., Niehof, J.T., de Pater, I., Lissauer, J.L., 2004. Microwave observations of Saturn's rings: Anisotropy in directly transmitted and scattered saturnian thermal emission. Icarus 171, 183–198.

Dunn, D.E., de Pater, I., Wright, M., Hogerheijde, M.R., Molnar, L.A., 2005. High-quality BIMA-OVRO images of Saturn and its rings at 1.3 and 3 millimeters. Astron. J. 129, 1109–1116.

Ferrin, I., 1975. On the structure of Saturn's rings and the "real" rotational period for the planet. Astrophys. Space Sci. 33, 453–457.

Franklin, F.A., Colombo, G., 1978. On the azimuthal brightness variations of Saturn's rings. Icarus 33, 279–287.

Franklin, F.A., Cook, A.F., Barrey, R.T.F., Roff, C.A., Hunt, G.E., de Rueda, H.B., 1987. Voyager observations of the azimuthal brightness variations in Saturn's rings. Icarus 69, 280–296.

French, R.G., Nicholson, P.D., 2000. Saturn's Rings. II. Particle sizes inferred from stellar occultation data. Icarus 145, 502–523.

French, R.G., Dones, L., Salo, H., 2000. HST observations of the azimuthal brightness asymmetry in Saturn's rings. Bull. Am. Astron. Soc. 32, 864.

French, R.G., McGhee, C.A., Dones, L., Lissauer, J.J., 2003. Saturn's wayward shepherds: The peregrinations of Prometheus and Pandora. Icarus 162, 143–170.

French, R.G., McGhee, C.A., Frey, M., Hock, R., Rounds, S., Jacobson, R., Verbiscer, A., 2006. Astrometry of Saturn's satellites from the Hubble Space Telescope WFPC2. Publ. Astron. Soc. Pacific 118, 246–259.

Goldreich, P., Lynden-Bell, D., 1965. II. Spiral arms as sheared gravitational instabilities. Mon. Not. R. Astron. Soc. 130, 125–158.

Hedman, M.M., Nicholson, P.D., Salo, H., Wallis, B.D., Buratti, B.J., Baines, K.H., Brown, R.H., Clark, R.N., 2007. Self-gravity wake structures in Saturn's A ring revealed by Cassini VIMS. Astron. J. 133, 2624–2629.

Julian, W.H., Toomre, A., 1966. Non-axisymmetric responses of differentially rotating disks of stars. Astrophys. J. 146, 810–830.

Karjalainen, R., Salo, H., 2004. Gravitational accretion of particles in Saturn's rings. Icarus 172, 328–348.

Karttunen, H., 1983. The wake model for azimuthal brightness variations in Saturn's A-ring. Moon Planets 29, 117–120.

Lewis, M.C., Stewart, G.R., 2005. Expectations for Cassini observations of ring material with nearby moons. Icarus 178, 124–143.

Lissauer, J.J., French, R.G., 2000. HST high-resolution backscatter image of Saturn's G ring. Icarus 146, 12–18.

Lumme, K., 1970. On photometric properties of Saturn's rings. Astrophys. Space Sci. 8, 90–101.

Lumme, K., Esposito, L.W., Irvine, W.M., Baum, W.A., 1977. Azimuthal brightness variations of Saturn's rings. II. Observations at an intermediate tilt angle. Astrophys. J. 216, L123–L126.

Lumme, K., Irvine, W.M., 1976. Azimuthal brightness variations of Saturn's rings. Astrophys. J. 204, L55–L57.

Lumme, K., Irvine, W.M., 1979a. A model for the azimuthal brightness variations in Saturn's rings. Nature 282, 695–696.

Lumme, K., Irvine, W.M., 1979b. Azimuthal brightness variations of Saturn's rings. III. Observations at tilt angle B approximately equal to 11.5 deg. Astrophys. J. 229, L109–L111.

Marouf, E.A., Tyler, G.L., Zebker, H.A., Simpson, R.A., Eshleman, V.R., 1983. Particle size distributions in Saturn's rings from Voyager 1 radio occultation. Icarus 54, 189–211.

Marouf, E., French, R., Rappaport, N., McGhee, C., Wong, K., Thomson, F., 2005. Cassini radio occultation results for Saturn's rings. Eos (Fall Meet.) 86 (52). Abstract P31D-04.

Marouf, E.A., French, R.G., Rappaport, N.J., McGhee, C.A., Wong, K., Thomson, F.S., Anabtawi, A., 2006. Structure and properties of Saturn's ring B from Cassini radio occultations. Bull. Am. Astron. Soc. 38. Abstract 38.05.

McGhee, C.A., Nicholson, P.D., French, R.G., Hall, K.J., 2001. HST observations of saturnian satellites during the 1995 ring plane crossings. Icarus 152, 282–315.

McGhee, C.A., French, R.G., Dones, L., Cuzzi, J.N., Salo, H.J., Danos, R., 2005. HST observations of spokes in Saturn's B ring. Icarus 173, 508–521.

Molnar, L.A., Dunn, D.E., Niehof, J.T., 1999. Fall 1998 Radio observations of Saturn's rings: New evidence of ring wakes. Bull. Am. Astron. Soc. 31. Abstract 44.05.

Molnar, L.A., Crull, E.M., Dunn, D.E., 2004. A and B ring wakes in high dynamic range radio maps of Saturn. Bull. Am. Astron. Soc. 36, 1917.

Nicholson, P., French, R.G., Campbell, D.B., Margot, J.-L., Nolan, M.C., Black, G.J., Salo, H., 2005a. Radar imaging of Saturn's rings. Icarus 177, 32–62.

Nicholson, P.D., Hedman, M.M., Wallis, B., Cassini VIMS Team, 2005b. Cassini-VIMS observations of stellar occultations by Saturn's rings. Bull. Am. Astron. Soc. 37, 763.

Ohtsuki, K., Emori, H., 2000. Local N-body simulations for the distribution and evolution of particle velocities in planetary rings. Astron. J. 119, 403–416.

Pérez-Hoyos, S., Sánchez-Lavega, A., French, R.G., Rojas, J.F., 2005. Saturn's cloud structure and temporal evolution from ten years of Hubble Space Telescope images (1994–2003). Icarus 176, 155–174.

Porco, C.C., Throop, H.B., Richardson, D.C., 2001. Light scattering in Saturn's rings: Basic disk properties and the A ring azimuthal asymmetry. Bull. Am. Astron. Soc. 33, 1091–1092.

Porco, C.C., and 34 colleagues, 2005. Cassini imaging science: Initial results on Saturn's rings and small satellites. Science 307, 1226–1236.

Poulet, F., Cuzzi, J.N., French, R.G., Dones, L., 2002. A study of Saturn's ring phase curves from HST observations. Icarus 158, 224–248.

Price, M.J., 1973. Optical scattering properties of Saturn's rings. Astron. J. 78, 113–120.

Reitsema, H.J., Beebe, R.F., Smith, B.A., 1976. Azimuthal brightness variations in Saturn's rings. Astron. J. 81, 209–215.

Richardson, D.C., 1994. Tree code simulations of planetary rings. Mon. Not. R. Astron. Soc. 269, 493–511.

Rosen, P.A., Tyler, G.L., Marouf, E.A., 1991. Resonance structures in Saturn's rings probed by radio occultation. I. Methods and examples.. Icarus 93, 3–24.

Salo, H., 1992. Gravitational wakes in Saturn's rings. Nature 359, 619–621.

Salo, H., 1995. Simulations of dense planetary rings. III. Self-gravitating identical particles. Icarus 117, 287–312.

Salo, H., Karjalainen, R., 1999. Dynamical and photometric modeling of azimuthal brightness asymmetry in Saturn's rings. Bull. Am. Astron. Soc. 31, 1160.

Salo, H., Karjalainen, R., 2003. Photometric modeling of Saturn's rings. I. Monte Carlo method and the effect of non-zero volume filling factor. Icarus 164, 428–460.

Salo, H., Karjalainen, R., French, R.G., 2000. Modeling the azimuthal brightness asymmetry in Saturn's rings. Bull. Am. Astron. Soc. 32, 864.

Salo, H., Schmidt, J., Spahn, F., 2001. Viscous overstability in Saturn's B-ring. I. Direct simulations and measurement of transport coefficients. Icarus 153, 295–315.

Salo, H., Karjalainen, R., French, R.G., 2004. Photometric modeling of Saturn's rings. II. Azimuthal asymmetry in reflected and transmitted light. Icarus 170, 70–90.

Sánchez-Lavega, A., Pérez-Hoyos, S., Acarreta, J.R., French, R.G., 2002. No hexagonal wave around Saturn's southern pole. Icarus 160, 216–219.

Sánchez-Lavega, A., Pérez-Hoyos, S., Rojas, J.F., Hueso, R., French, R.G., 2003. A strong decrease in Saturn's equatorial jet at cloud level. Nature 423, 623–625.

Sánchez-Lavega, A., Hueso, R., Pérez-Hoyos, S., Rojas, J.F., French, R.G., 2004. Saturn's cloud morphology and zonal winds before the Cassini encounter. Icarus 170, 519–523.

Schmidt, J., Salo, H., 2003. Weakly non-linear model for oscillatory instability in Saturn's dense rings. Phys. Rev. Lett. 90, 061102.

Schmit, U., Tscharnuter, W., 1995. A fluid dynamical treatment of the common action of self-gravitation, collisions, and rotation in Saturn's B-ring. Icarus 115, 304–319.

Schmidt, J., Salo, H., Spahn, F., Petzschmann, O., 2001. Viscous overstability in Saturn's B-Ring. II. Hydrodynamic theory and comparison to simulations. Icarus 153, 316–331.

Seiß, M., Spahn, F., Sremčević, M., Salo, H., 2005. Structures induced by small moonlets in Saturn's rings: Implications for the Cassini Mission. Geophys. Res. Lett. 32, 11205.

Showalter, M.R., Nicholson, P.D., 1990. Saturn's rings through a microscope—Particle size constraints from the Voyager PPS scan. Icarus 87, 285–306.

Showalter, M.R., Bollinger, K.J., Nicholson, P.D., Cuzzi, J.N., 1996. The rings node for the planetary data system. Planet. Space Sci. 44, 33–45.

Thompson, W.T., 1982. The swarm model for the azimuthal brightness variations in Saturn's ring A. Ph.D. thesis. Univ. of Massachusetts, Amherst.

Thompson, W.T., Lumme, K., Irvine, W.M., Baum, W.A., Esposito, L.W., 1981. Saturn's rings—Azimuthal variations, phase curves, and radial profiles in four colors. Icarus 46, 187–200.

Thomson, F., Wong, K., Marouf, E., Rappaport, N., French, R., McGhee, C., 2005. Scattered signal observations during Cassini radio occultations by Saturn's rings. In: AGU Fall Meeting Abstracts, P33B-0247.

Tiscareno, M.S., Burns, J.A., Hedman, M.M., Porco, C.C., Weiss, J.W., Dones, L., Richardson, D.C., Murray, C.D., 2006. 100-metre-diameter moonlets in Saturn's A ring from observations of 'propeller' structures. Nature 440, 648–650.

Toomre, A., 1964. On the gravitational stability of a disk of stars. Astrophys. J. 139, 1217–1238.

Toomre, A., 1981. What amplifies the spirals. In: Fall, M., Lynden-Bell, D. (Eds.), Structure and Evolution of Normal Galaxies. Cambridge Univ. Press, Cambridge, UK, pp. 111–136.

Toomre, A., Kalnajs, A.J., 1991. Spiral chaos in an orbital patch. In: Sundelius, B. (Ed.), Dynamics of Disc Galaxies. Almquist-Wiksell, Göteborg, pp. 341–358.

Trauger, J.T., Vaughan, R.W., Evans, R.W., Moody, D.C., 1995. Geometry of the WFPC2 focal plane. In: Koratkar, A., Leitherer, C. (Eds.), Calibrating Hubble Space Telescope: Post Servicing Mission. Space Telescope Science Institute, Baltimore, MD, pp. 379–385.

van der Tak, F.E., de Pater, I., Silva, A., Millan, R., 1999. Time variability in the radio brightness distribution of Saturn. Icarus 142, 125–147.

Verbiscer, A.J., French, R.G., McGhee, C.A., 2005. The opposition surge of Enceladus: HST observations 338–1022 nm. Icarus 173, 66–83.

Weidenschilling, S.J., Chapman, C.R., Davis, D.R., Greenberg, R., 1984. Ring particles—Collisional interactions and physical nature. In: Planetary Rings. IAU Colloq. 75. CEPADUES-Editions, pp. 367–415.

Wisdom, J., Tremaine, S., 1988. Local simulations of planetary rings. Astron. J. 95, 925–940.

Wong, K.K., Marouf, E.A., 2004. Cassini radio occultation of Saturn's rings: A Bayesian approach to particle size distribution recovery. In: AGU Fall Meeting Abstracts, A1457.